Friedrich-Alexander-Universität
Erlangen-Nürnberg

Department für Physik
Lehrstuhl für Physik

D I P L O M A R B E I T

Gamma-Hadron-Separation in the Mono Regime of the H.E.S.S. II Experiment

Martin Hupfer

Eingereicht am: 5. Dezember 2008

Gutachter: 1. Prof. Dr. Ch. Stegmann
2. Prof. Dr. U. Katz

Abstract

The High Energy Stereoscopic System (H.E.S.S.) is an array of four imaging Cherenkov telescopes, situated in the Namibian Khomas Highlands, which aims at studying very high-energy cosmic γ-rays ($E > 100\,\mathrm{GeV}$). In order to achieve a lower energy threshold and higher sensitivity of the array, a fifth, larger telescope is currently under construction (H.E.S.S. phase II), which will be able to detect photons with energies as low as 20 GeV due to its larger mirror area. In contrast to the H.E.S.S. I telescopes, the camera of the large telescope will be capable of measuring the time of the maximum signal in each pixel. In order to reject the strong background of charged hadrons for events which trigger exclusively the large telescope (mono events), new methods for gamma-hadron separation are needed. This diploma thesis aims at finding and evaluating new separation methods on the basis of Monte-Carlo simulations of the H.E.S.S. II array, making use of the information available about the time structure of the camera images.

In a first step, the timing information is used to achieve better image cleaning. It is shown that the different image cleaning algorithm leads to a more complete image of the observed air shower in the camera, especially for low energies. Subsequently, the image parameters used in the H.E.S.S. I analysis are amended by additional image parameters, suited for gamma-hadron separation. The time-development of images in the camera is investigated and it is shown that they are not suited for separation due to too strong fluctuations.
Finally, a neural network is used to obtain an optimal separation based on the available parameters and the influence of the new image cleaning, as well as the influence of a preselection cut on the image's position in the camera is studied. An approximation for the gain in the significance of a source by the separation cut on the neural net output is the quality factor η. For a cut, which is optimised on the quality factor, the maximum value of η is 4.44 without, and 3.38 after a preselection cut. The improvements by the new image cleaning are shown to be 17% and 8% respectively.

Kurzfassung

Das High Energy Stereoscopic System (H.E.S.S.) ist ein System aus vier abbildenden Cherenkov Teleskopen im Khomas Hochland von Namibia, welches der Untersuchung hochenergetischer kosmischer γ-Strahlung dient ($E > 100\,\mathrm{GeV}$). Um die Energieschwelle des Systems zu senken, und eine höhere Sensitivität zu erzielen, wird zur Zeit ein fünftes, größeres Teleskop gebaut (H.E.S.S. Phase II), das auf Grund seiner größeren Spiegelfläche in der Lage sein wird auch Photonen mit Energien ab ca 20 GeV nachzuweisen. Im Gegensatz zu den bisherigen H.E.S.S. I Teleskopen, erlaubt die Kamera des großen Teleskops, auch die Zeit, zu der die Intensität maximal ist, für jeden Pixel zu messen. Um den starken Hintergrund an geladenen Hadronen auch für Ereignisse zu unterdrücken, welche allein das große Teleskop detektiert (mono Ereignisse), sind neue Methoden zur Gamma-Hadronen Separation notwendig. Ziel dieser Diplomarbeit ist die Erprobung neuer Separationsmethoden anhand von Monte-Carlo Simulationen des H.E.S.S. II Teleskopes, unter Verwendung der verfügbaren Zeitinformation der Kamerabilder.

In einem ersten Schritt wird die Zeitinformation verwendet, um die Bildbereinigung der Kamerabilder effektiver durch zu führen. Es wird gezeigt, dass vor allem im Niederenergiebereich die neue Bildbereinigung zu einer vollständigeren Abbildung der beobachteten Luftschauer führt. Anschließend werden die bereits in der H.E.S.S. I Analyse verwendeten Bildparameter um einige weitere zur Separation geeignete Parameter erweitert. Die zeitliche Entwicklung der Kamerabilder wird untersucht und es wird gezeigt, dass sich diese auf Grund zu starker Fluktuation nicht zu Separation eignen.
Ein neuronales Netz wird abschließend verwendet, um eine optimale Separation anhand der zur Verfügung stehenden Größen zu erreichen, und der Einfluss der neuen Bildbereinigung, sowie eines Auswahlschnittes auf die Lage des Bildes in der Kamera untersucht. Eine Näherung für den, durch den Separationsschnitt auf den Ausgabewert des neuronalen Netzes erreichten Verbesserungsfaktor der Signifikanz einer Quelle ist der quality factor η. Für einen auf den quality factor optimierten Separationsschnitt ergibt sich ein maximaler Wert für η von 4.44 ohne, sowie von 3.38 nach dem Auswahlschnitt. Der Zuwachs durch die neue Bildbereinigung beläuft sich dabei auf 17% bzw. 8%.

Contents

0 Introduction

Until the 20th century, astronomy was limited to the exploration of our universe in the optical band of electromagnetic radiation. This was due to the fact that the earth's atmosphere is opaque for most other wavelengths. It was only through the rapid technological advancement of the 20th century that astronomers were able to expand their research to other bands of the electromagnetic spectrum. Using very large radio-telescopes and satellite experiments, the field of astronomy today covers more than 20 orders of magnitude of the electromagnetic spectrum, instead of only 1 in the early 20th century.

Especially the observation of VHE γ-rays (very high energy; $E > 10\,\mathrm{GeV}$) in modern gamma-ray astronomy promises to deliver insights into some of the universe's most violent environments, as photons of such enormous energies can only be produced by non-thermal emission processes. These processes, during which a large amount of the available energy is focused onto a small number of particles, are still subject to theoretical research. The experimental techniques to study this radiation, however, are challenging as well [1].

In 1912, during balloon experiments, the Austrian physicist Victor Franz Hess discovered the existence of a strongly ionising radiation, which grew stronger with increasing altitude. It is well known today that the energy spectrum $N(E)$ of this radiation - called cosmic rays (CR) - covers more than 11 orders of magnitude, ranging from $10^9\,\mathrm{eV}$ to up to $10^{20}\,\mathrm{eV}$, following a power law:

$$\frac{\mathrm{d}N(E)}{\mathrm{d}E} \propto E^{-\Gamma}.$$

The spectral index Γ is 2.7, except for the range of 10^{15} to $10^{18}\,\mathrm{eV}$, where the spectrum decreases more rapidly and $\Gamma = 3.1$ [2]. The rapidly decreasing flux (only 1 particle per square meter and second at $10\,\mathrm{GeV}$) makes it impossible to study VHE γ-rays with satellite experiments, as the detection area of satellites is restricted to just a few square meters. Furthermore, CR consist of more than 99% charged particles, which are deflected in galactic and inter-galactic magnetic fields and therefore hit the earth isotropically. Only the small amount of uncharged particles (neutrinos and photons) contains information about their origin and is therefore of primary interest for astronomers.

As the hadronic CR background for all known sources outweighs the photonic signal, γ-ray astronomy is always dominated by background, with signal to noise ratios of usually $\approx 1/1000$. It is therefore necessary to develop methods to seperate the small signal from the large background. Due to all these problems, up until 2003 only the order of 10 sources of VHE γ-rays were identified. The last decades have however seen great progress in the field of astro-particle physics and especially in ground-based γ-ray astronomy, which led to the discovery of more than 60 new sources of VHE γ-rays [3]. Figure 0.1 shows all known sources of TeV emission. While most sources have counterparts in other electromagnetic bands such as supernova remnants or pulsar wind nebulae, some sources remain as of yet unidentified.

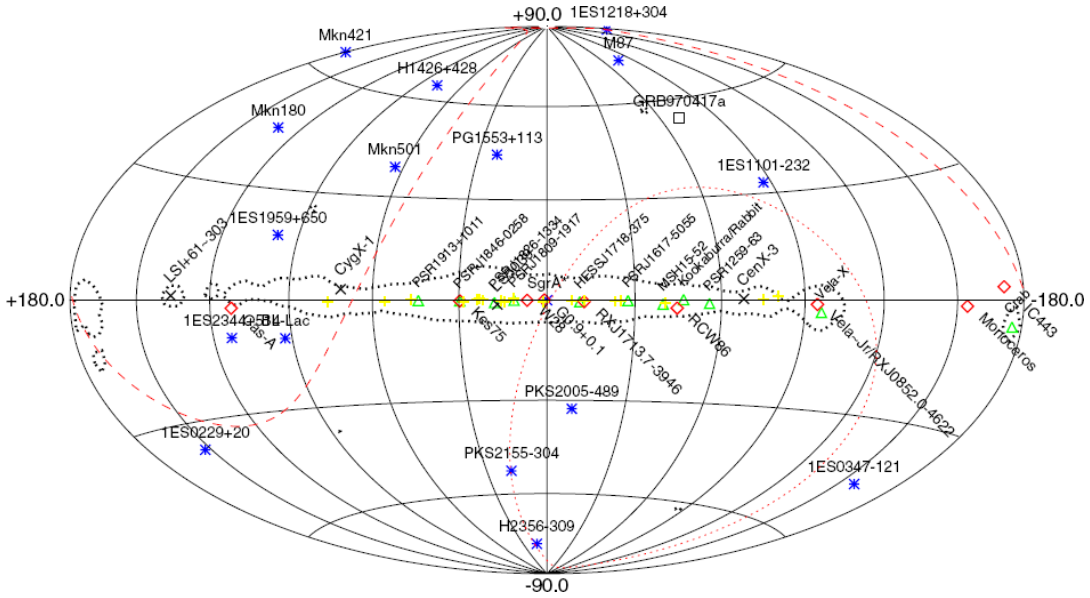

Fig. 0.1: *Sources of TeV emission in galactic coordinates. Blue stars represent extragalctic sources while yellow crosses indicate unidentified sources (from [3])*

While ground-based γ-ray experiments such as the High Energy Stereoscopic System (H.E.S.S., an array of four Imaging Atmospheric Cherenkov Telescopes), MAGIC, VERITAS and CANGAROO can detect VHE γ-ray sources and study their spectral properties in the energy range of 50 GeV to 100 TeV, satellite experiments have in the past been sensitive for energies up to 10 GeV. At the moment, efforts to close this gap between satellite and ground based experiments are under way. New satellite experiments such as the Large Area Telescope on board the Fermi Gamma-ray Space Telescope (formerly GLAST) are able to detect photons with energies of up to 300 GeV [4]. At the same time a new, larger telescope is being built at the H.E.S.S. site (H.E.S.S. phase II), which will be sensitive to γ-rays with energies as low as 20 GeV due to it's large reflector area.

Since normally the H.E.S.S. array uses stereoscopic information, i.e. information from the different persepectives of the four telescopes, to separate the photonic signal from the hadronic background, new methods are neccessary to reduce the background for the large telescope to a sensible level, as for low energy events only the large telescope will trigger due to its lower energy threshold. This thesis presents and evaluates methods for γ-hadron separation for these single-telescope (mono) events. At first, an overview of the detection principle of Imaging Atmospheric Cherenkov Telescopes and the H.E.S.S. experiment will be given. After a brief summary of the H.E.S.S. I methods for γ-hadron separation, new methods for γ-hadron separation will be introduced and their suitability for single-telescope events will be tested. Finally the methods will be optimised for use on a point source and the quality of the separation cut will be evaluated.

1 Ground-Based Gamma-Ray Astronomy

Currently the most succesful technique for detecting VHE γ-rays are ground-based Imaging Atmospheric Cherenkov Telescopes (IACTs). These Telescopes observe the moonless night sky, looking for short flashes of ultraviolet / blue Cherenkov light emitted by particle cascades (called air showers) which are induced by VHE γ-rays entering the atmosphere. The camera image of the shower is then used to reconstruct both the direction of the shower (resulting in the location of the source) and the energy of the primary particle (used to construct the spectral properties of the source).
While the advantage of this technique lies in the huge effective detection area, which is made possible by using the atmosphere as a detector, it has to cope with the problem that these cascades show large fluctuations due to the enormous amount of individual interactions involved in the shower development. Furthermore, Cherenkov light is not only emitted by showers induced by γ-rays, but also by cascades induced by the hadronic background that hits the atmosphere isotropically.
The following Section illustrates the basic physical properties of air showers and of the Cherenkov emmission associated with them. Afterwards, a short overview over the detection principle of IACTs is given.

1.1 The Physics of Air Showers

1.1.1 Electromagnetic Air Showers

Whenever a VHE γ-ray hits the atmosphere and induces an electromagnetic air shower, the shower development is dominated by three processes: pair production, Bremsstrahlung and ionisation. The cascade is initiated when the primary photon undergoes pair production in the electromagnetic field of an atmospheric nucleus and thereby creates an electron-positron pair, which then moves through the upper atmosphere. These two leptons will in turn emit Bremsstrahlung while traversing other nuclei's electromagnetic field and thus create new photons, which will again undergo pair production. This cycle holds as long as the energy of the photons emitted by Bremsstrahlung is larger than the threshold energy for pair production:

$$E_{min} = 2m_e c^2 \left(1 + \frac{m_e}{M}\right) \approx 1.02\,\mathrm{MeV},$$

where m_e and M are the masses of electron and nucleus. The expression $\left(1 + \frac{m_e}{M}\right)$ takes into account the loss of energy during the interaction due to the transfer of momentum to the nucleus. While $\frac{m_e}{M}$ is quite small for nuclei and can be neglected, it leads to an increase in E_{min} for pair production near lightweight particles like electrons.
The cascade will grow until the energy of the leptons drops below the critical energy of $E_c = 80\,\mathrm{MeV}$, where energy loss by ionisation of air molecules becomes the dominant effect over bremsstrahlung. No further Bremsstrahlung photons will be created and the shower

expires. The lateral spread of electromagnetic showers is governed by multiple Coulomb scattering of the charged leptons off nuclei. The contribution of pair production and especially of Bremsstrahlung can be neglected since for example most of the Bremsstrahlung photons are emitted in a narrow cone in the forward direction with an average opening angle of $\langle\Theta\rangle = 1/\gamma$, where γ denotes the Lorentz factor.

The atmospheric depth, at which the shower reaches its maximum is governed by the energy loss of the VHE leptons by Bremsstrahlung, which is given by:

$$-\left(\frac{\mathrm{d}E}{\mathrm{d}x}\right) = \frac{E(x)}{X_0} \iff E(x) = E_0 \cdot \mathrm{e}^{-\frac{x}{X_0}}. \tag{1.1}$$

X_0 denotes the radiation length, i.e. the path length after which the particle's energy has dropped to 1/e of its initial energy E_0. The radiation length is given in units of the integrated density $\rho(h)$ along the path:

$$X_0 = \int_{h_0}^{\infty} \rho(h)\mathrm{d}h.$$

and is approximately $37.2\,\mathrm{gcm}^{-2}$ for electrons in air. For pair production, the corresponding length is called mean free path length, which in air is approximately $\frac{9}{7}X_0$ [5]. The atmospheric depth x_{max} at which the shower reaches its maximum number of particles is reached when the mean energy of the shower electrons has dropped to E_c and is therefore given by:

$$E_c = E(x_{max}) = E_0 \cdot \mathrm{e}^{-\frac{x_{max}}{X_0}}$$

$$\Rightarrow x_{max} = \ln\left(\frac{E_0}{E_c}\right) \cdot X_0. \tag{1.2}$$

The important point of Equation 1.2 is that x_{max} shows a logarithmic dependency on the initial energy E_0.

Simple Shower Model

A simple shower model introduced by Bethe and Heitler can be used to describe some additional properties of electromagnetic showers [7]. It assumes that both radiation length for leptons and mean free path length for γ-rays are equal (given by X_0) and that the primary particle's energy is in each interaction divided equally between both secondary particles. Moreover, X_0 now denotes the length after which a new interaction occurs, so that X_0 in this model describes the atmospheric depth after which an electron or positron loses half of its energy (compared to 1/e for the real radiation length). The basic properties of the model are visualised in Figure 1.1.

Since at each interaction (occuring after the shower has penetrated one radiaton length deeper into the atmosphere) the number of particles in the shower, N_p, is doubled, the number of particles grows exponentially with the atmospheric depth, while the mean energy of each particle E_p decreases exponentially:

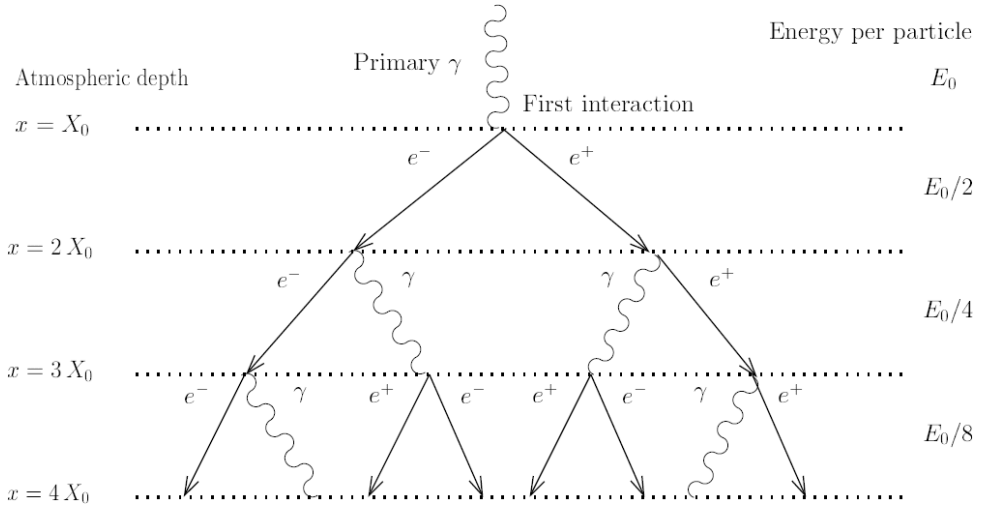

Fig. 1.1: *Simple electromagnetic shower model (Bethe and Heitler, taken from [6]).*

$$N_p(x) = 2^n \quad \text{with} \quad n = \frac{x}{X_0} \tag{1.3}$$

$$E_p = E_0 \cdot 2^{-n}.$$

This particle cascade grows until E_p drops below the critical Energy E_c, after which energy loss by ionisation becomes dominant, as mentioned above. Since ionisation is neglected by this simple shower model, it cannot describe the further shower development. At the shower maximum however, this model can be used to calculate the maximum number of particles, as well as the atmospheric depth at which the shower maximum occurs:

$$E_c = E_0 \cdot 2^{-\frac{x_{max}}{X_0}}$$

$$\Rightarrow x_{max} = \frac{\ln(E_0/E_c)}{\ln 2} X_0 \tag{1.4}$$

$$N_{max} = 2^{\frac{x_{max}}{X_0}} = \frac{E_0}{E_c} \tag{1.5}$$

Although the model is quite simple, Equations 1.3 - 1.5 reflect some of the most important properties of an electromagenetic shower:

- the exponential growth of the Number of Particles,
- the proportionality of N_{max} to the primary's energy E_0,
- the proportionality of x_{max} to $\ln E_0$.

1.1.2 Hadronic Air Showers

Whereas for electromagnetic showers only pair production, bremsstrahlung and ionisation contribute to the shower development, the situation for hadronic showers is far more

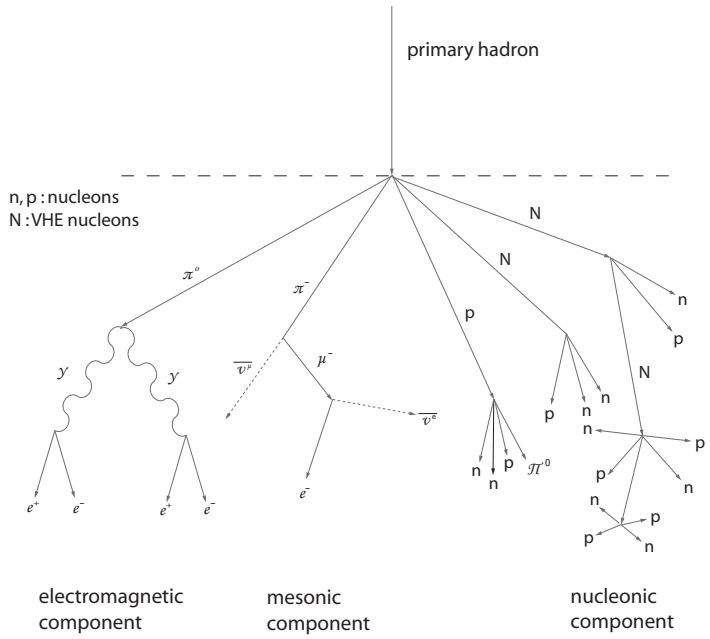

Fig. 1.2: *Exemplary evolution of a hadronic cascade including electromagnetic, muonic and hadronic component (courtesy of Sebastian Heinz).*

complex. Protons and nuclei interact predominantly via the strong interaction. The most frequent interaction is inelastic scattering of the hadrons off atmospheric nuclei, whereby mesons, like pions and kaons, as well as nucleons and hyperons are produced.
While the charged pions decay to long-lived neutrons and muons which in part escape from the shower region, the uncharged π^0-mesons decay quickly to two photons which induce electromagnetic sub-showers (compare Figure 1.2).

The most important points distinguishing hadronic from electromagnetic showers are as follows (compare [8, page 14]):

- The larger mean free path length of protons in air ($80\,\mathrm{gcm}^{-2}$ for $E = 1$ TeV) compared to photons ($48\,\mathrm{gcm}^{-2}$) leads to a larger penetration depth of hadronic showers in the atmosphere.
- Since a significant fraction of the primary particle's energy is transferred to muons or neutrinos or dissipated in interactions between nuclei, hadronic showers need the threefold energy to generate the same number of particles in electromagnetic sub-showers as do γ-induced showers.
- The complex strong interactions involved in the shower development lead to larger fluctuations of hadronic showers (see Figure 1.3).
- The inelastic scattering processes of hadrons on complex targets (like nuclei) lead to a larger transfer of transverse momentum (compared to multiple Coulomb scattering) and thus a larger lateral spread of the shower (see Figure 1.3).

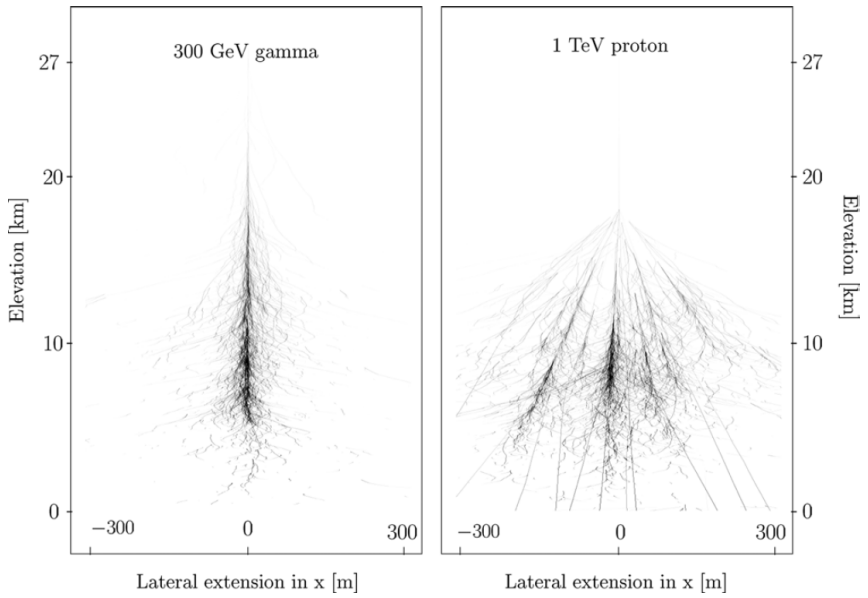

Fig. 1.3: *Comparison of the shower development for a leptonic and a hadronic shower (taken from [3]). While the electromagnetic shower (left side) shows only a small lateral spread compared to its longitudinal extension, the hadronic shower (right side) is quite a lot more extended and also more irregular in shape.*

1.1.3 Cherenkov Emission

Cherenkov photons are emitted whenever a charged particle moves through a medium with a velocity v greater than the local speed of light $c' = c/n$ (where n denotes the refractive index of the medium). The charged particle polarizes the atoms along its path which emit photons when returning to their equilibrium state. For velocities smaller than the speed of light the electromagnetic radiation interferes destructively, while for $v > c'$ the interference is additive (See Figure 1.4). This effect is equivalent to the shock front of a supersonic boom. All photons are emmited in a cone with an opening angle of:

$$\vartheta_C = \arccos\frac{c'}{v} = \arccos\frac{1}{n\beta} \quad \text{with} \quad \beta = \frac{v}{c}.$$

Since the particles in air showers travel at highly relativistic velocities they emit Cherenkov light which can be measured by ground-based telescopes. The requirement $v > c'$ leads to a threshold energy, above which particles with mass m_0 emit Cherenkov photons:

$$E_{th} = \frac{m_0 c^2}{\sqrt{1 - n^{-2}}}.$$

Since $E_{th} \propto m_0$, most of the Cherenkov radiation is emitted by leightweight particles such as electrons and positrons. Concerning the opening angle of the Cherenkov cone emitted by a shower, one has to take into account that the refractive index of air varies with its density ρ, which is a function of the height above sea level z. The deviation η of the refractive index from 1 ($\eta = n - 1$) is proportional to the density:

$$\eta \propto \rho(z) \approx \rho_0 \exp(-z/z_\rho) \tag{1.6}$$

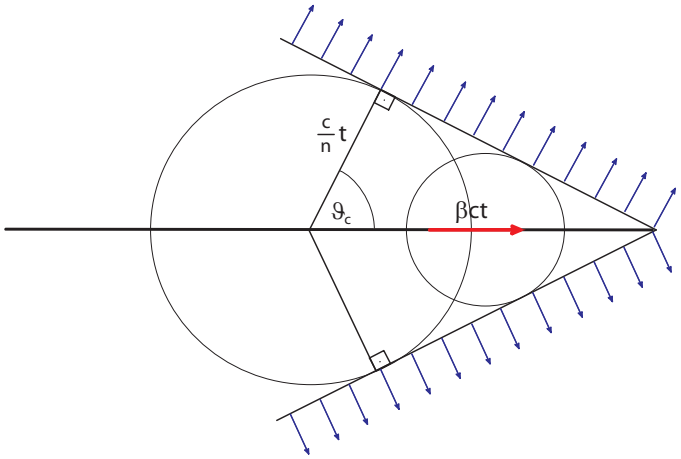

Fig. 1.4: *Emission of Cherenkov light: in the time t the emitting particle travels the distance βct while the emitted light travels the distance $c/n \cdot t$. For $\beta c > c/n$ the light is emitted in a forward cone with opening angle ϑ_C.*

where $\rho_0 \approx 1.205 \cdot 10^{-3}\,\mathrm{gcm}^{-3}$ and $z_\rho \approx 8.5\,\mathrm{km}$. Therefore $\eta(z)$ is approximately given by:

$$\eta(z) \approx \eta_0 \exp(-z/z_0) \tag{1.7}$$

where $\eta_0 = 2.9 \cdot 10^{-4}$ and $z_0 = 7250\,\mathrm{m}$, which deviates slightly from the standard scale height of air, z_ρ, in Equation 1.6 (compare [3]). The changing refractive index, as well as the retardation of the shower particles due to their decreasing energy leads to a dependency of ϑ_C of the shower height z. ϑ_C ranges from $\approx 0.3°$ to $1°$, which results in a smearing of the Cherenkov light registered at ground level. Figure 1.5 shows the simulated distribution of the Cherenkov light on the ground for a 300 GeV γ-ray shower (left) and for a 1 TeV proton shower (right). While the electromagnetic shower illuminates a ring of $\approx 250\,\mathrm{m}$ diameter, the light distribution of the hadronic shower reflects the large fluctuations as well as the numerous sub showers typical for hadronic showers.

1.2 Imaging Atmospheric Cherenkov Technique

As described in the section above, the Cherenkov light from an electromagnetic shower iluminates a circular region on the ground of $\approx 250\,\mathrm{m}$ in diameter. It is therefore possible to image the shower by using ground-based telescopes (IACTs). With approximately $50000\,\mathrm{m}^2$ of detection area, IACTs allow to study VHE γ-rays up to energies of as much as 100 TeV. In order to achieve a low energy threshold, it is advisable to use telescopes with a large mirror area to detect the faint flashes of Cherenkov light emitted by low energy air showers. For a 1 TeV electromagnetic shower, for example, only ≈ 200 Cherenkov photons per square meter reach the ground.

Figure 1.6 illustrates the mapping of the shower onto the camera in the focal plane. The picture on the left side shows the optical path of the Cherenkov light emitted at three different times in the shower development which is focused onto the telescope camera. The picture on the right side shows the corresponding camera image. Light emitted at the

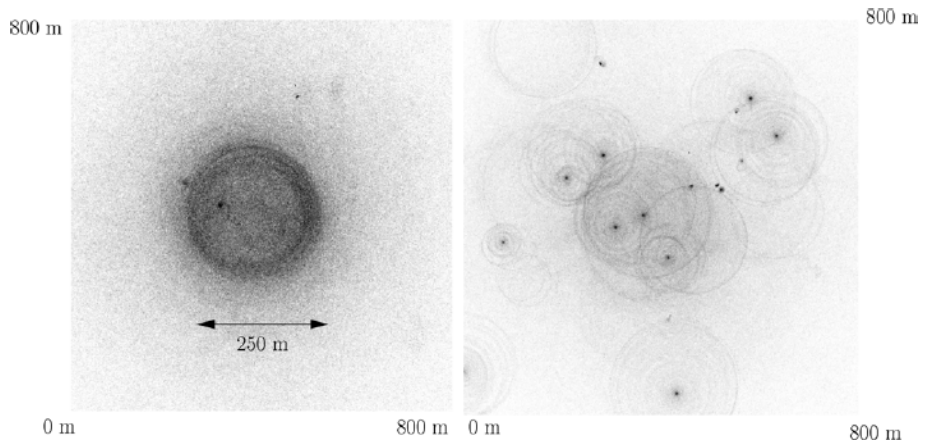

Fig. 1.5: *Distribution of Cherenkov photons on the ground level (taken from [3]). While an electromagnetic shower ($E = 300\,\mathrm{GeV}$) iluminates a circle with approximately 250 m diameter (left side) the distribution is far more irregular for a hadronic shower (right side, $E = 1\,\mathrm{TeV}$).*

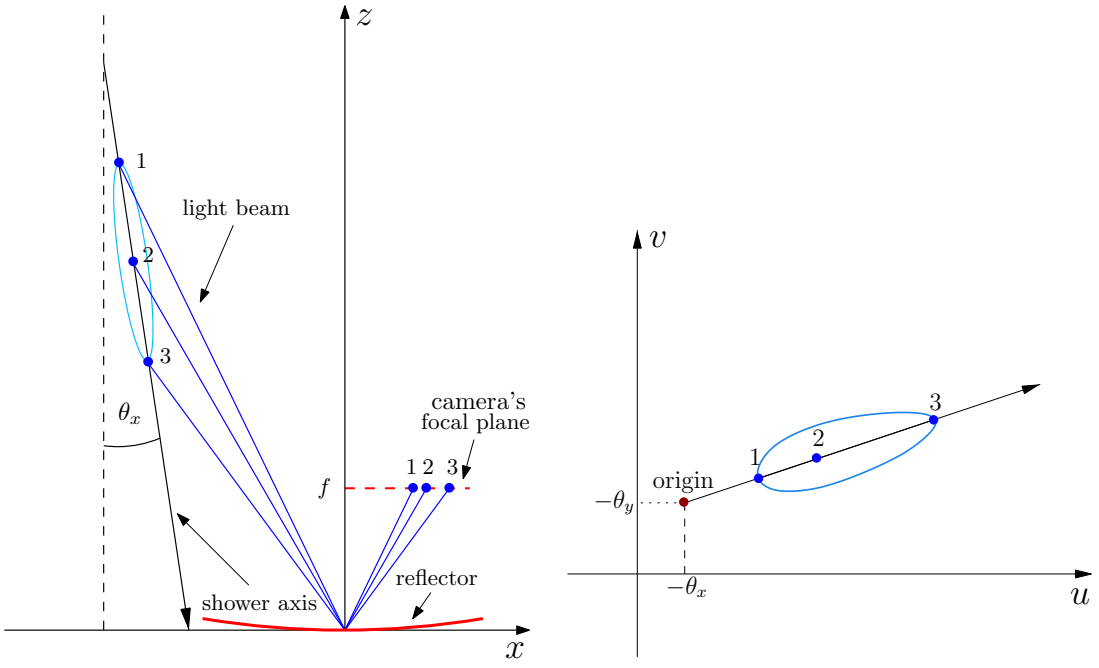

(a) Mapping of an air shower.

(b) Corresponding camera image.

Fig. 1.6: *Detection of VHE γ-rays with an IACT. The shower is mapped onto the camera in the focal plane of the reflector (left side) which results in a slightly distorted elliptical image of the air shower (right side).*

place (x, y, z) during the shower development is mapped onto the coordinates (u, v) in the camera plane, which are given by:

$$\begin{pmatrix} u \\ v \end{pmatrix} = -\frac{f}{z} \begin{pmatrix} x \\ y \end{pmatrix}, \tag{1.8}$$

where f is the focal length of the telescope. The shower images are by approximation ellipses, but distorted by the nonlinearity of the mapping. This distortion is however usually neglected, and the shower images are described as ellipses. Since the distortion does not affect the allignment of the image's major axis (which is the image of the shower axis) this assumption has no effect on the reconstruction of the source position, which can be found along the image's major axis (compare Figure 1.6).

Stereoscopic arrays of IACTs, like the H.E.S.S. experiment in Namibia, instead of single IACTs, allow to obtain a more precise measurement of the shower parameters, since the shower is observed from different positions. Furthermore, stereoscopic arrays allow to reduce the muonic background, since muons emit Cherenkov light only in a very small cone, so that one muon is very unlikely to trigger more than one telescope. Further advantages are an improved sensitivity of the array, as well as a better gamma-hadron separation due to the additional information available from the different telescopes.

Single IACTs, like the MAGIC I experiment on Las Palmas, have, however, usually larger telescope reflector areas as only one telescope has to be built. Since a larger part of the Cherenkov photons incident on ground level is focused into the camera, this allows for detection of weaker Cherenkov flashes originating from photons with lower energy and resulting in a usually lower energy threshold of single IACTs.

2 The H.E.S.S. Experiment

The High Energy Stereoscopic System (H.E.S.S.) is an array of Cherenkov telescopes situated in the Khomas Highlands of Namibia at 1800 m above sea level. This site was chosen because of the good conditions for astronomical observations in this very arid environment (57% of moon-less nights are cloud-free). Furthermore, the experiment's location in the southern hemisphere is optimal for observations of the Galactic Plane.
Since 2003 the experiment has consisted of four IACTs (H.E.S.S. Phase I) working in stereoscopic mode. A fifth, larger IACT is currently under construction on the H.E.S.S. site and will be operational in 2009 (H.E.S.S. Phase II).

2.1 H.E.S.S. Phase I

The H.E.S.S. Phase I experiment consists of four IACTs arranged in a square of 120 m side length (Figure 2.1). This spacing allows for optimal stereoscopic viewing conditions, while still being small enough to keep multiple telescopes in the Cherenkov light pool of a single shower.

Each telescope has a reflector area of $107\,\mathrm{m}^2$ consisting of 382 round mirrors of $60\,\mathrm{cm}^2$ diameter arranged in a Davies-Cotton design (i.e. a sphere, which has a radius of 15 m for the H.E.S.S. I telescopes), which is suited for observations off the telescopes main axis.
The reflector is mounted on an Alt-Azimuth mount, which can track sources from elevations of 20° to 89.9°. The pointing accuracy of the H.E.S.S. I telescopes is better than 30".

The Cherenkov light hitting the reflector is focused on a camera consisting of 960 pixels. These pixels are comprised of Winston cones which collect the incident light and focus it onto photo multiplier tubes (PMTs) with a quantum efficiency of $\approx 15\%$. Each pixel has a field of vision of 0.16°, which leads to a total field-of-view of the telescope of $\approx 5°$.
Each camera is divided into 38 overlapping sectors of 64 pixels each, and the telescope is

Fig. 2.1: *The H.E.S.S. I Telescope Array in the Gamsberg Area of the Khomas Highlands in Namibia.*

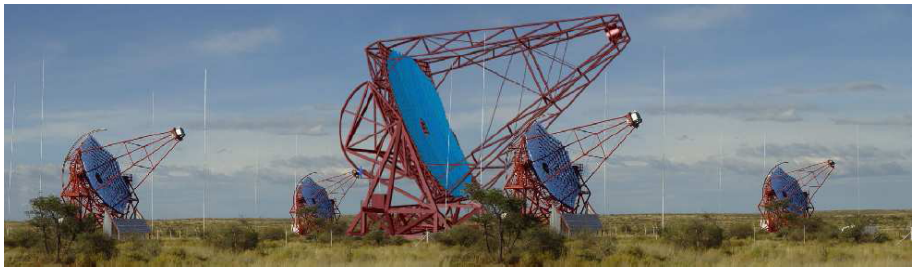

Fig. 2.2: *A computer generated image of the future H.E.S.S. II Telescope Array (taken from [9]).*

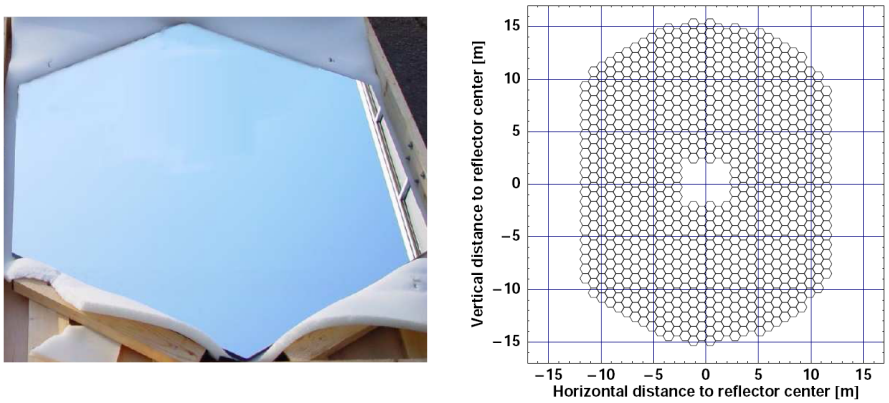

Fig. 2.3: *One of the hexagonal H.E.S.S. II mirror facets (left) which will be arranged in a parabolic shape of* 24×30 *m (right, taken from [9] and [10]).*

triggered if more than 4 pixels in one sector exceed a threshold of 4 photo electrons (pe) in a time interval of ≈ 1.3 ns. The signal of each pixel is then integrated over 16 ns and a trigger signal is sent to a central trigger, which demands that at least 2 telescopes have been triggered in 80 ns.

The H.E.S.S. I array achieves an energy threshold of ≈ 100 GeV and is able to reconstruct the origin of a γ-ray with an accuracy of $0.1°$. The energy resolution is of the order of 15% to 20%. The flux sensitivity of the array is 1% of the Crab nebula flux, meaning that a source with an integrated flux of 1% of the Crab nebula can be detected in 25 h of observation time.

2.2 H.E.S.S. Phase II

Currently, a fifth telescope is under construction at the H.E.S.S. site in Namibia. With 600 m^2 of reflector area and a weight of approximately 560 tons it will be the largest IACT ever built. It will be located in the middle of the existing H.E.S.S. I array and is expected to be operational in 2009 (see Figure 2.2).

The telescope's reflector differs in some aspects from the reflector layout used for the smaller H.E.S.S. telescopes. It comprises 850 hexagonal mirror facets (90 cm flat to flat) arranged in a parabolic shape with a focal length of 36 m (Figure 2.3). The reason for the different mirror layout compared to the H.E.S.S. I telescopes (parabolic instead of spherical

design) is that the Davies-Cotton spherical design, while optimizing off axis observations, leads to a time dispersion in the photons forming the image. This time dispersion is proportional to the focal length (for a fixed ratio of reflector size and focal length) and would lead to an unacceptable time dispersion of a few nanoseconds [10].

The reflector is mounted on an Alt-Azimuth dish comparable to those of the smaller telescopes. A quadrupod supports the H.E.S.S. II camera, consisting of 2048 hexagonal pixels (each comprising a PMT and a Winston Cone). Each pixel covers a field of vision of 0.07°, leading to a total field-of-view of the H.E.S.S. II telescope of 3.2°. The camera is divided into 96 sectors of 64 PMTs and uses a trigger identical to the H.E.S.S. I trigger: at least N pixels (usually 5) in one sector have to exceed a variable threshold (e.g. 3.5 pe) in a short time inteval of a few ns. When the telescope is triggered it records the pixel intensites as well as the time of the maximum signal ($T0$) and the time over a defined threshold (ToT) for an integration range of 16 ns. The signal is read with a sampling frequency which can be varied between 500 MHz and 3 GHz (for more information see [9]).

2.3 Monte-Carlo Simulations

Since the new telescope (CT5) will not be operational until 2009, all studies presented in this diploma thesis are based on Monte-Carlo simulations of the H.E.S.S. II array.

The CORSIKA[1] package was used for the simulation of air showers. It considers various aspects that are important for the shower development like the geomagnetic field strength in the atmosphere or atmospheric absorption of the Cherenkov light. It also provides different atmospheric models, of which a desert model is usually used to simulate the arid weather conditions of the Namibian highlands.
While electromagnetic showers can be simulated using Quantum Electrodynamics (QED), the simulation of the manifold hadronic interactions in hadronic showers requires different models developed by particle physics experiments. For different energy regimes, different interaction models are used, among them VENUS, QGSJET and SIBYLL.

The propagation of the simulated Cherenkov photons into the camera is done using sim_hessarray [12]. This complex detector simulation takes into account the entire detection process, e.g.:

- the reflector layout,
- the shadowing of mirrors due to the support structure,
- the mirror reflectivity,
- the transmission of the Winston Cones,
- the quantum efficiency of the PMTs,
- the trigger condition.

Furthermore, the simulation includes the noise due to the Night Sky Background (NSB) by asigning each pixel a NSB photoelectron rate, as well as the white noise generated by the electronics.

[1] COsmic Ray SImulations for KAscade, for information see [11]

The Monte-Carlo simulations used in this thesis were generated for an observation position south of the telescopes at 20° zenith angle. The reflectivity of the mirrors of CT1-4 (the H.E.S.S. I telescopes) was assumed to be 50% (degraded by the desert winds), while CT5 was simulated with a mirror reflectivity of 100%.

3 Gamma-Hadron Separation

This chapter introduces quantities which can be used to evaluate the separation power of an algorithm and of the separation potential inherent in different variables. Furthermore, it gives a short overview of the standard H.E.S.S. I separation methods and successively introduces the methods used for gamma-hadron separation in CT5 single-telescope events in this thesis.

3.1 Measuring Separation Power

Three important quantities, which can be used to evaluate the gamma-hadron separation power of different variables and algorithms are the separation, the significance and the quality factor. Section 3.1.1 introduces the separation, which is a measure for the separation potential of different variables, while Section 3.1.2 introduces the significance of a source, as well as the quality factor, which is a quantity describing the gain in significance achieved by a separation algorithm.

3.1.1 The Separation

One possible way of describing the separation potential inherent in any characteristical variable y is to measure the overlap of the variable's distributions for signal (γ-rays) and background (hadrons). Figure 3.1 shows the distributions of two exemplary variables

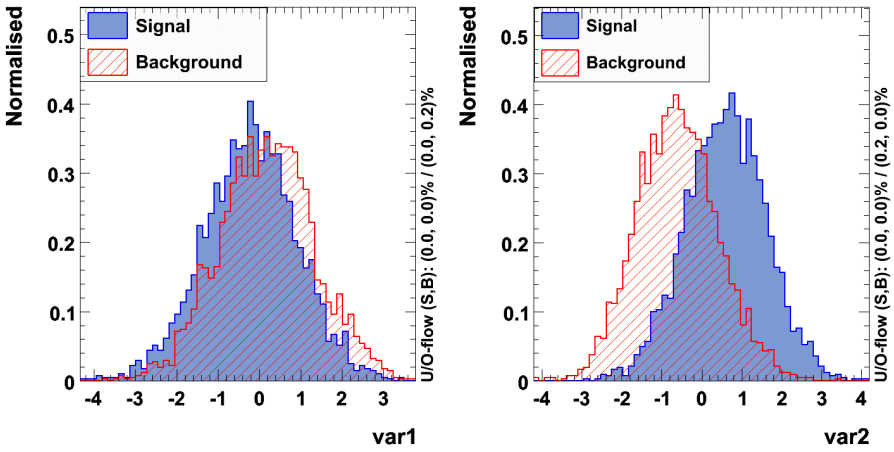

Fig. 3.1: *Two exemplary variables and their distributions for signal and background events. While var1 (left panel) shows only a small separation between signal and background, var2 (right panel) is far better suited to distinguish between signal and background (resulting in a larger separation).*

var1 and var2 for both signal and background. While the distribution of var1 is almost identical for signal and background, the distributions of var2 show a smaller overlap, which makes them better suited to distinguish background and signal. A quantity measuring the overlap of the distributions of a variable y for signal ($\hat{y}_S(y)$) and background ($\hat{y}_B(y)$) is the *separation* $\langle S^2 \rangle$ defined by [13, page 19]:

$$\langle S^2 \rangle := \frac{1}{2} \int \frac{(\hat{y}_S(y) - \hat{y}_B(y))^2}{\hat{y}_S(y) + \hat{y}_B(y)} \mathrm{d}y. \tag{3.1}$$

For identical signal and background shapes the separation is 0, while for distributions with no overlap the separation is 1. For the exemplary varibles in Figure 3.1, the separation is 0.27 for var2 but only 0.038 for var1. The separation is therefore suited to decide on which variables to use for gamma-hadron separation.

3.1.2 Significance and Quality Factor

The significance of a source is a measure used in astronomy to describe the probability that an observed signal is caused by fluctuations of the cosmic-ray background, and not by a source. For gamma-ray astronomy, which is typically dominated by background, it is reasonable to optimise separation algorithms for a maximum increase of the significance of a source.

Figure 3.2 shows the typical observation method used in γ-ray astronomy. A test position (on region) is observed for a time t_{on}. In order to estimate the background, a second observation is made with the telescopes pointing at a position in the sky where presumably no source is located with a duration of t_{off}. The estimated number of background events for the observation of the on region $\langle N_B \rangle$ can then be calculated by:

$$\langle N_B \rangle = \alpha N_{\mathrm{off}},$$

where $\alpha = t_{\mathrm{on}}/t_{\mathrm{off}}$. Note that for some observations the size of the on and off regions may not be the same. Furthermore the two regions can be mapped at different places in the camera with a different camera acceptance. These aspects are usually also included in the scaling factor α.

The number of excess events N_S during the observation, which is given by

$$N_S = N_{\mathrm{on}} - \alpha N_{\mathrm{off}},$$

is used to calculate the significance S of the observed excess:

$$S = \frac{N_S}{\sigma(N_S)}, \tag{3.2}$$

which is the deviation of the excess counts from their expectation value 0, in units of their standard deviation $\sigma(N_S)$, under the assumption that the excess is only caused by fluctuations of the background. The hypothesis to have no source in the FoV is usually rejected above deviations of 5 sigma.

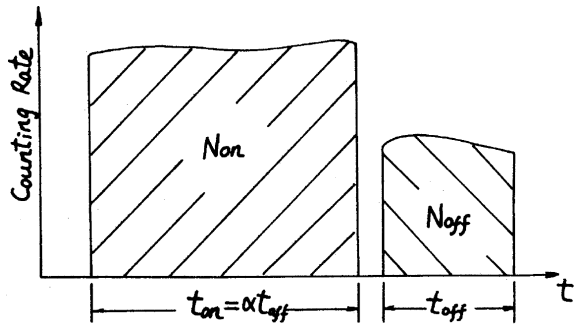

Fig. 3.2: *The typical observation method used in γ-ray astronomy [14]. The test region (on region) is observed for the time t_{on}. Afterwards the background is estimated by observing an empty region (off region).*

Since N_{on} and N_{off} are two independent measurements, the variance $\sigma^2(N_S)$ of N_S is given by:

$$\sigma^2(N_S) = \sigma^2(N_{\text{on}}) + \sigma^2(\alpha N_{\text{off}}) = \underbrace{\sigma^2(N_{\text{on}})}_{\langle N_B \rangle} + \alpha^2 \underbrace{\sigma^2(N_{\text{off}})}_{\langle N_B \rangle / \alpha}$$

$$\Rightarrow \sigma^2(N_S) = (1+\alpha)\langle N_B \rangle, \tag{3.3}$$

where the fluctuation of the background was assumed to be Poisson distributed, so that the variance is given by the expectation value. A better estimate for $\langle N_B \rangle$ (than αN_{off}) can be gained by using both the on and the off region to calculate $\langle N_B \rangle$. Assuming that no source is located in the on region, $\langle N_B \rangle$ is given by:

$$\langle N_B \rangle = \frac{N_{\text{on}} + N_{\text{off}}}{t_{\text{on}} + t_{\text{off}}} \cdot t_{\text{on}} = \frac{\alpha}{1+\alpha}(N_{\text{on}} + N_{\text{off}}),$$

which, together with Equation 3.3, yields for the significance:

$$S = \frac{N_S}{\sqrt{\alpha(N_{\text{on}} + N_{\text{off}})}}. \tag{3.4}$$

For the observation of a γ-ray source, where the excess events are given by the number of γ-rays N_γ and the background by the number of cosmic rays N_{CR}, as well as under the assumptions $\alpha = 1$ and $N_\gamma \ll N_B$, Equation 3.4 reads:

$$S = \frac{N_\gamma}{\sqrt{N_\gamma + 2N_{CR}}} \approx \frac{N_\gamma}{\sqrt{2N_{CR}}}. \tag{3.5}$$

If we now apply an algorithm for gamma-hadron separation (for example a simple cut on a discriminating variable), the algorithm will not only sort out many background events, but some of the signal events as well. With N being the number of events before the cut and $\hat{N}$ the number of events passing the cut, the signal (background) efficiency is defined as the percentage of events passing the cut:

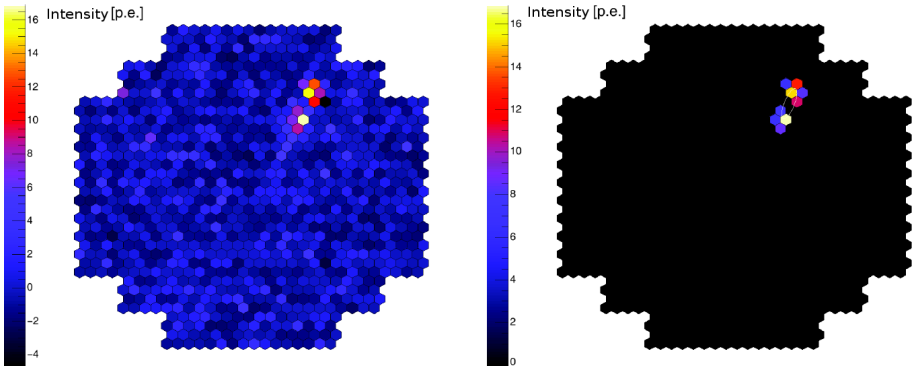

Fig. 3.3: *Camera image of an event before (left side) and after tailcut image cleaning (right side).*

$$\epsilon_\gamma = \frac{\hat{N}_\gamma}{N_\gamma} \ , \ \epsilon_{CR} = \frac{\hat{N}_{CR}}{N_{CR}}.$$

The significance of the source after cuts is now given by:

$$\hat{S} = \frac{\hat{N}_\gamma}{\sqrt{2\hat{N}_{CR}}} = \frac{\epsilon_\gamma}{\sqrt{\epsilon_{CR}}} \cdot \frac{N_\gamma}{\sqrt{2N_{CR}}} = \underbrace{\frac{\epsilon_\gamma}{\sqrt{\epsilon_{CR}}}}_{=:\eta} \cdot S. \tag{3.6}$$

The factor $\eta := \frac{\epsilon_\gamma}{\sqrt{\epsilon_{CR}}} = \frac{\hat{S}}{S}$ is called *quality factor* and quantifies the gain of significance achieved by the separation algorithm. The quality factor will therefore be used to evaluate the performance of all separation algorithms in this thesis.

3.2 H.E.S.S. I

In order to allow for a comparison of the methods used for gamma-hadron separation for H.E.S.S. II mono and for H.E.S.S. I stereoscopic events, and to stress the similarities and differences between the two methods, the next section will give a short overview of the standard H.E.S.S. I image cleaning and separation methods.

3.2.1 Tailcut Image Cleaning

The images recorded by the H.E.S.S. cameras do not exclusively depict the air showers, but are an overlay of the shower image and noise created by the night sky background and by the camera electronics. In order to separate the shower image from the rest of the image, a tailcut is applied: only pixels with an amplitude exceeding 10 pe which are adjacent to a pixel with more than 5 pe, or pixels with more than 5 pe adjacent to a pixel with more than 10 pe are kept in the image, while all other pixels are regarded as background and discarded from the image. It should be noted that for the standard tailcut image cleaning of CT5 mono events in this thesis a more relaxed cut was appplied, which demands that the pixel intensity exceeds 7 pe (4 pe) with an ajdacent pixel of at least 4 pe (7 pe).

Figure 3.3 shows the camera image of a recorded event before tailcuts (left) and after tailcuts (right). While this cut technique is very efficient at supressing the background, it also leads to a loss of information due to low intensity pixels at the border of the shower being deleted from the image. This is a significant effect for small images, where these cuts result in the image being smaller than expected, which results in a bias on the reconstructed energy (since the shower's energy is assumed to be proportional to the number of photo electrons in the image).

3.2.2 Image Parametrisation

Due to the large longitudinal spread of air showers and their small lateral spread, the cleaned camera images resemble ellipses. The shape of these ellipses is usually described by the first and second moments of the images intensity distribtion. The characteristic parameters used to describe the ellipse and its orientation in the camera are called *Hillas parameters* and were first proposed by A. M. Hillas in 1985 [15].
Figure 3.4 depicts the entire set of Hillas parameters. The first moment of the intensity distribution is called the center of gravity (CoG) of the ellipse. The matrix of second moments yields the *length* and *width* of the ellipse, as well as the direction of the images major axis, which is parametrised via the angle Φ. Further Hillas parameters are the total *size* of the image in photo electrons, and the angle α between the major axis and the connecting line between the CoG and the camera centre. For more information on the calculation of the Hillas parameters see [6].

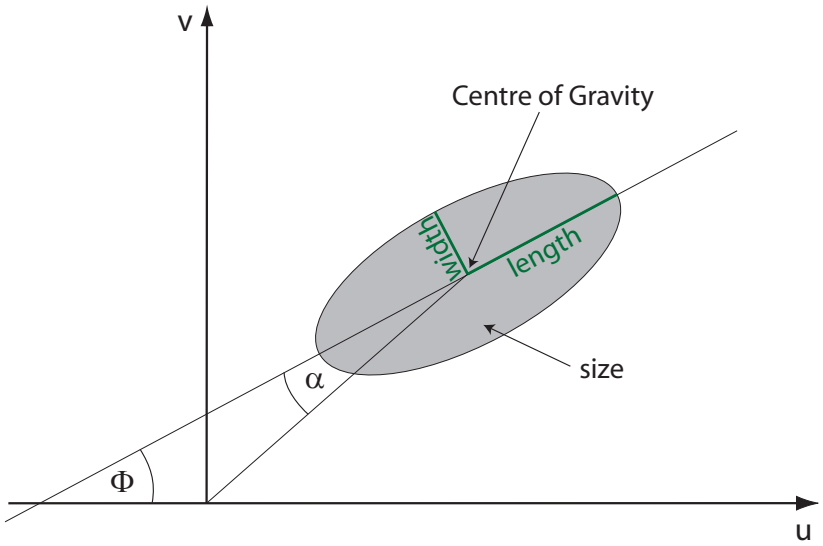

Fig. 3.4: *The entire set of Hillas parameters describing shape, position and orientation of the camera image.*

As mentioned in Section 1.1.2, the most pronounced difference between electromagnetic and hadronic showers is the different spread of the shower. This leads to a larger *width* and *length* of hadronic showers compared to γ-induced showers. However, the *length* and *width* of a shower image is also dependent on the energy of the shower ($N_{max} \propto E$), which is mirrored in the Hillas parameter *size*, and on the distance of the impact point of the shower axis on ground level to the telescope, called *impact parameter* (showers which are farther away seem smaller in the telescope). Taking this into account, the image is not ideally

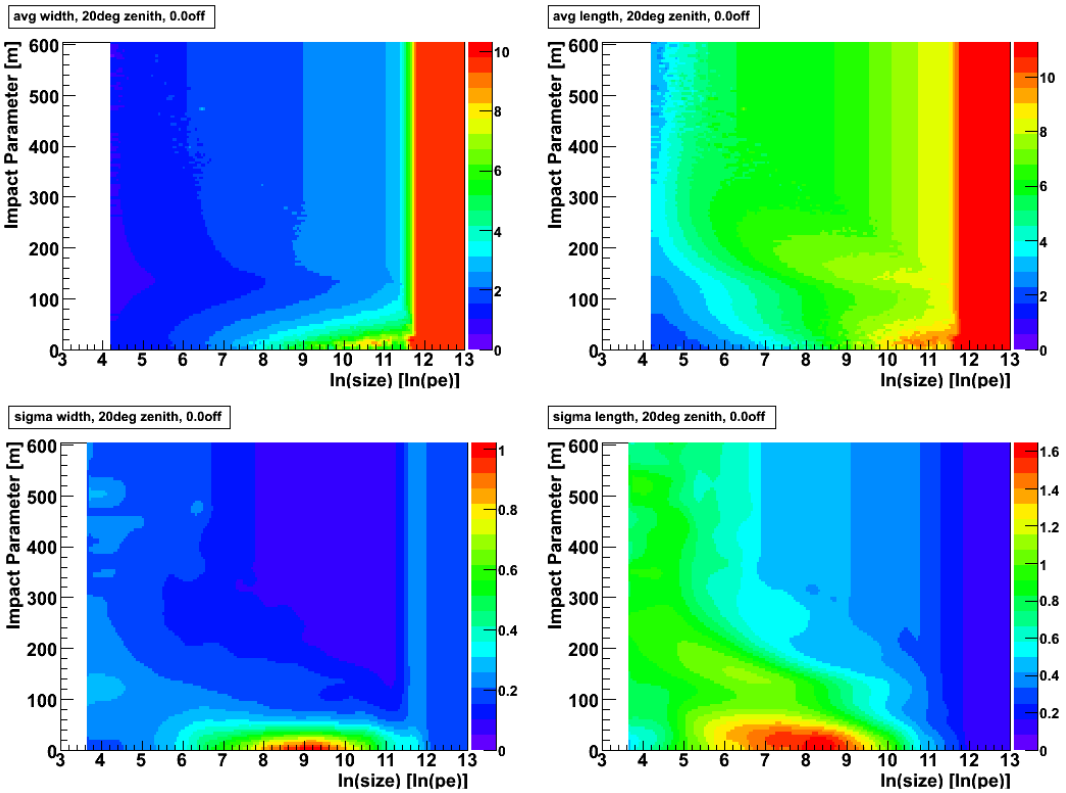

Fig. 3.5: *Lookup tables for average width and length in mrad for γ-ray events as a function of the impact parameter and image size for 20° zenith angle and 0.0° offset (top row, left and right). The bottom row shows the corresponding errors due to the fluctuations of the shower.*

described by the parameters *length* and *width*, but better by the Mean Reduced Scaled Width (Length) called *MRSW* (*MRSL*), which is the mean deviation of the *width* (*length*) from the expectation value $\langle width \rangle$ for an electromagnetic shower with a certain *size* and impact parameter in units of its standard deviation $\sigma(width)$. Monte-Carlo simulations are used to calculate these expectation values as well as their standard deviation for different zenith angles and different offsets of the source in the camera (i.e. that the source position is not located at the camera centre, but located at a small angular distance from the camera centre, called offset), and stored in histograms which are called lookup tables (see Figure 3.5).

In order to calculate *MRSW* (*MRSL*), the reduced scaled width (length) *RSW* (*RSL*) for each telescope i is calculated by:

$$RSW_i = \frac{width_i - \langle width_i \rangle}{\sigma(width_i)}.$$

The Mean Reduced Scaled Width (Length) of an event is then given by:

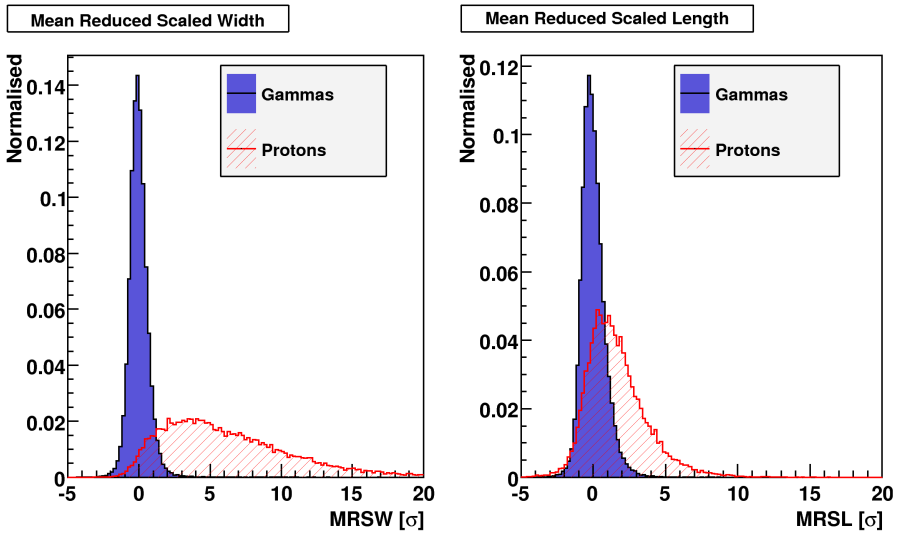

Fig. 3.6: *Mean reduced scaled width (left side) and length (right side) for Monte-Carlo gammas and protons. While for γ-induced showers the distributions are normally distributed, hadronic showers lead to longer and especially wider images.*

$$MRSW = \frac{\sum_{i=1}^{N_{\text{tels}}} (RSW_i \cdot w_i)}{\sum_{i=1}^{N_{\text{tels}}} w_i}, \tag{3.7}$$

where w_i denotes the weight given to each telescope, which is given by

$$w_i = \frac{\langle width_i \rangle^2}{\sigma^2(width_i)}.$$

The distributions of *MRSW* and *MRSL* for γ and proton events is depicted in Figure 3.6. Since the distributions show only a small overlap between gammas and protons (especially for *MRSW*), these shower parameters are used to distinguish between γs and protons in the H.E.S.S. I analysis.

3.2.3 Event Selection Cuts

For the H.E.S.S. I analysis, two sets of cuts are applied to all events in order to select the γ-ray events from the large background and to choose only events which allow good reconstruction of the shower direction and energy.

- **Preselection cuts**: in a first step, all events which are either too small or too close to the camera edge are discarded from the analysis. Only images which a *size* parameter exceeding a variable threshold are kept, since for small images pixelisation effects lead to a rapidly deteriorating accuracy of the direction reconstruction. Furthermore, images with too large a *local distance* (distance from the camera centre to the *CoG* in m in the camera system) are also discarded since they possibly extend over the edge of the camera, resulting in too small a *size* parameter as well as bad reconstruction of the images major axis.

Cut	Image Size	θ^2	Local Distance	MRSW		MRSL	
	min.	max.	max.	min.	max.	min.	max.
Standard	80 p.e.	0.0125°	2°	-2.0	0.9	-2.0	2.0
Hard	200 p.e.	0.1°	2°	-2.0	0.7	-2.0	2.0
Loose	40 p.e.	0.4°	2°	-2.0	1.2	-2.0	2.0
Extended	80 p.e.	0.16°	2°	-2.0	0.9	-2.0	2.0

Table 3.1: *Overview of the different pre- and postselection cuts applied in the H.E.S.S. I analysis.*

Cut	No θ^2 γ %	No θ^2 CR %	η	All γ %	All CR %	η
Standard	49	2.4	3.2	35	9.4e-3	36
Hard	15	0.23	3.2	13	7.5e-4	47
Loose	84	9.2	2.8	68	0.11	21

Table 3.2: *Percentage of γ-ray ($\Gamma = 2.6$, zenith = 20°) and background events (zenith = 20°) passing selection cuts with and without a θ^2 cut, and the resulting quality factors [16].*

- **Postselection cuts**: after energy and direction reconstruction, the parameters *MRSW* and *MRSL* are calculated for all events passing the preselection cuts. All events with an either too small or too large value of *MRSW* and *MRSL* are discarded as protons. Furthermore, a cut on the squared angular distance between the reconstructed origin and assumed source position (θ^2) is applied, which discards a large percentage of proton events due to the isotropy of the cosmic-ray background.

For different types of sources, different thresholds are used for the pre- and postselection cuts. They are summarized in Table 3.1 and were chosen in order to optimise the significance per $\sqrt{\text{h}}$ for different source types. Table 3.2 shows the signal and background efficiency, as well as the quality factor achieved by the different cuts. The strongest factor for the discrimination of the background is the cut on θ^2. For further information on the H.E.S.S. I standard analysis see [16].

3.3 H.E.S.S. II Mono Regime

The following section presents the separation methods used in this thesis for gamma-hadron separation of H.E.S.S. II mono events. Special attention is paid to new methods based on the timing information recorded by the H.E.S.S. II camera.

3.3.1 Image Cleaning using Pixel Timining Information

As already mentioned in Section 3.2.1 the usual tailcut image cleaning used in the H.E.S.S. I analysis has the disadvantage of discarding signal pixels whose intensities are too low from the image. While for large images these discarded pixels can be neglected, as they form only a small part of the whole image, they lead to a considerable loss of information about

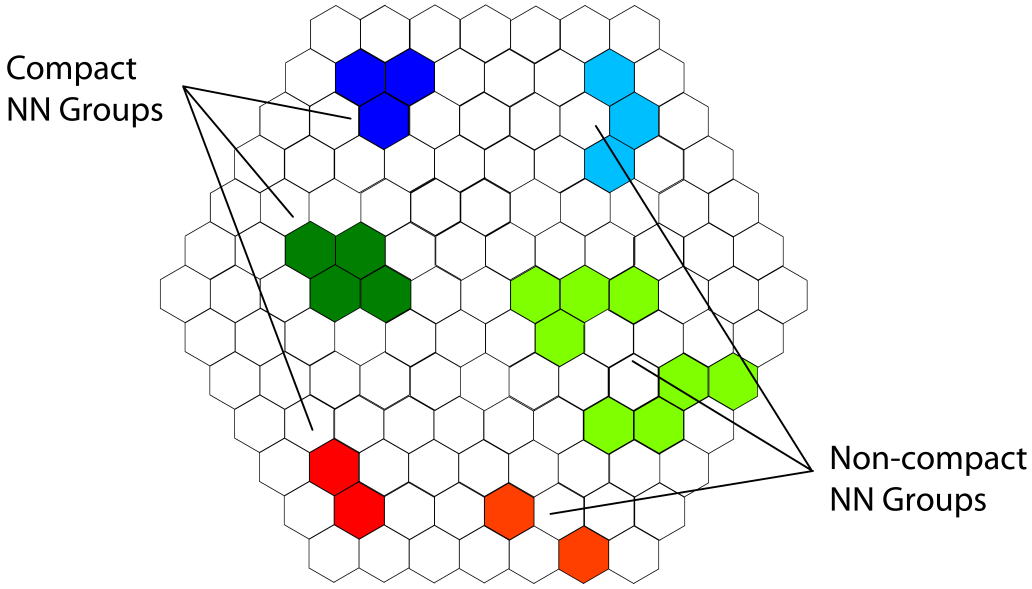

Fig. 3.7: *Schematic view of the inner region of a camera. While the highlighted pixel groups on the left side form compact next-neighbour groups, the groups on the right side are non-compact and not considered as signal pixels (after presentation associated with [17]).*

the shower for small images (and thus especially for the low-energy mono events).

The new layout of the CT5 camera enables us to use not only the topological information of the image for image cleaning (which is used by the tailcut cleaning), but also the image's time structure. This means that adjacent pixels do not only have to exceed a certain intensity threshold, but also that the arrival times of the light in both pixels have to be within a certain time window. While the arrival times for background photons are uniformly distributed, the difference in the arrival times for two adjacent signal pixels very seldomly exceeds 2 ns. The mean time difference is only ≈ 1 ns, see Figure 3.8 (right hand side). For background pixels the mean time difference is 2.5 ns. Moreover, 50% of the background pixels show a time difference of more than 2 ns. The MAGIC collaboration has developed a cleaning algorithm which makes use of both topological and timing information [17], which will be described in the following.

The camera image is scanned for compact next-neighbour (NN) groups which exceed a threshold intensity and are time correlated as well. Figure 3.7 shows compact groups consisting of two to four pixels (2NN, 3NN, 4NN) as well as pixel groups which are non-compact and excluded from the image. All compact NN groups which meet the requirements form the "core pixels" of the shower image. In a second step, all next-neighbours and second-next neighbours of core pixels are labeled as "boundary pixels" and checked again for time coincidence with the nearest core pixels (or boundary pixels for the second next-neighbour boundary pixels). Figure 3.8 shows the distribution of the intensity of background pixels (left hand side). It can be used to derive optimal threshold values for this cleaning algorithm. The NSB rate is however different for observations of different sky regions and therefore the thresholds used for image cleaning should depend on the observation. Table 3.3 summarises the cut values used for the image cleaning in this thesis.

Figure 3.9 shows the cleaned camera image of a γ-event after the standard tailcut image

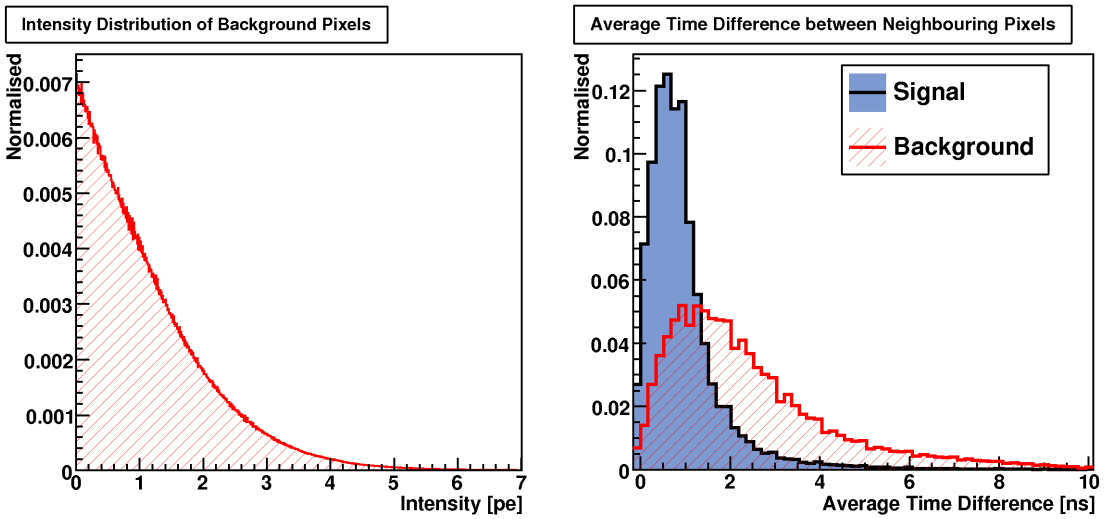

Fig. 3.8: *Distribution of the intensity of NSB (left side) and average time difference between neighbouring signal as well as background pixels (right side).*

Group	Intensity Threshold	ΔT
4NN	> 4 pe	< 3 ns
3NN	> 5 pe	< 3 ns
2NN	> 7 pe	< 1 ns
2NN	> 9 pe	whole window (16 ns)
Boundary (NN)	> 5 pe	whole window (16 ns)
Boundary (NN)	> 3 pe	< 2 ns
Boundary (2nd NN)	> 3 pe	< 2 ns

Table 3.3: *Criteria and thresholds used for image cleaning.*

cleaning (right side) and new image cleaning (left side). As can be seen, the two algorithms sometimes select different boundary pixels, while at the same time the overall shape of the image remains similar.

3.3.2 Hillas Parameters and Derived Quantities

The basic parameters applicable for gamma-hadron separation for single-telescope events are the Hillas Parameters, as defined in Section 3.2.2. While the *size* and local distance[1] of the image can be used to define preselection cuts, the *length*, *width*, local distance and α-parameter can be used for postselect gamma-hadron separation. Hadronic showers are uniformly distributed over the field of view, whereas the γ-induced showers originate at the source position (which for $0.0°$ offset is at the camera centre). Therefore, images of electromagnetic showers are usually centered between the camera center and edge (at a local distance of ≈ 0.4 m), while the images of hadronic showers are uniformly distributed in the camera plane, leading to a linear increase of the frequency of occurence of background images with local distance (due to the linear increase of the available area in the camera).
A cut on α can be used as a replacement for the θ^2-cut described in Section 3.2.3, until

[1] defined in Section 3.2.3

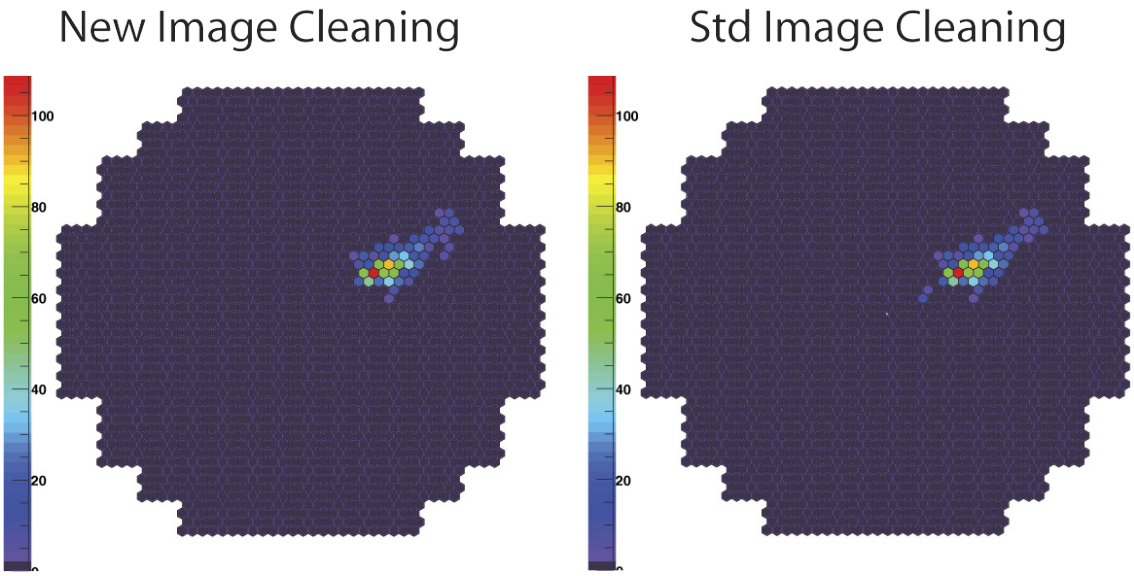

Fig. 3.9: *Camera images of the same γ-ray event after standard and new image cleaning.*

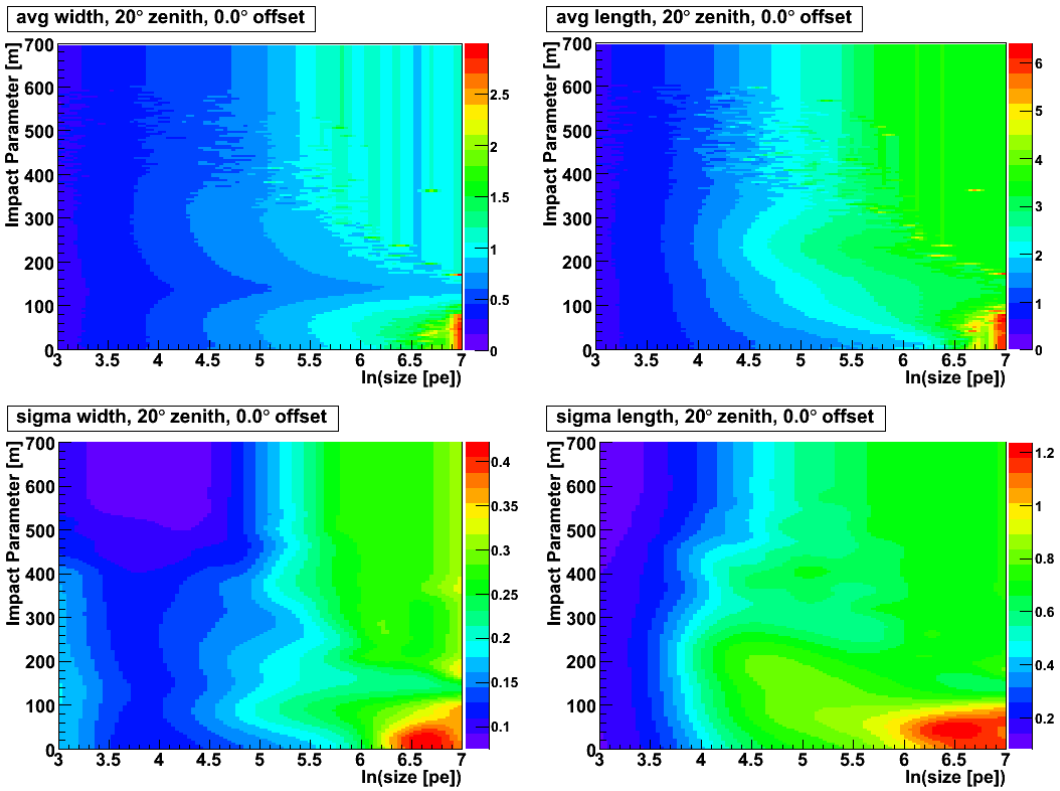

Fig. 3.10: *Lookup tables for average width and length for mono γ-ray events as a function of impact distance and image size for 20 deg zenith angle and 0.0 deg offset (top row, left and right). The bottom row shows the corresponding errors due to the fluctuations of the shower.*

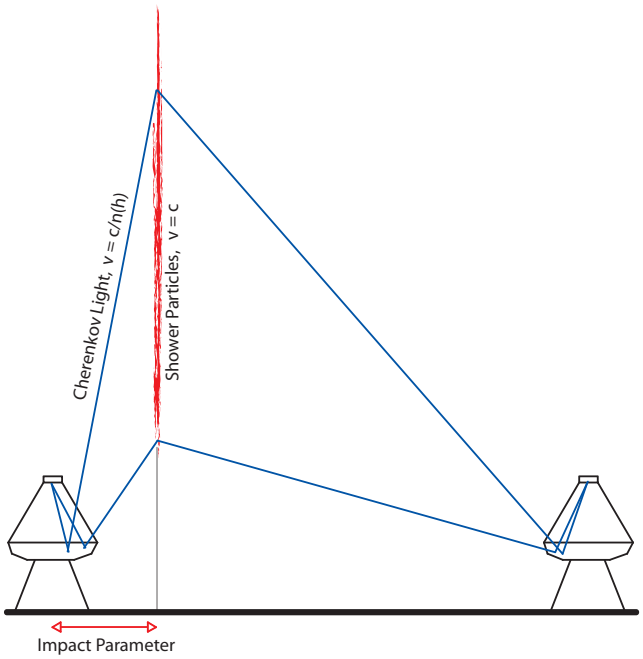

Fig. 3.11: *Propagation of light emitted at different stages of the development of an electromagnetic shower into two Cherenkov telescopes. While the emitted Cherenkov light travels with a velocity of $v = c/n(h)$, the shower front moves with a velocity close to the velocity of light for a long time. This leads to different shower developments in the cameras, since for small impact parameters, the Cherenkov light emitted at the shower's end arrives first, whereas for large impact parameters the light emitted at the shower's start arrives first.*

a final algorithm for single-telescop direction-reconstruction has been decided on. Since ideally the image's major axis should pass through the camera center, the angle α between the major axis and the connecting line between the image's CoG and the camera centre is a direct measure for the quality of the direction reconstruction. For this reason the distribution for α is peaked at 0° for γ-rays, while it is again uniformly distributed for protons between 0° and 90°.

The dependency of the *length* and *width* on the image *size* and on the impact parameter can again best be accounted for by using the RSW and RSL in analogy to the H.E.S.S. I selection cuts. Figure 3.10 shows the lookup tables for single-telescope events used for the calculation of RSW and RSL. Further parameters which have alread been used and tested for gamma-hadron separation are the ratio of the intensity contained in the three highest pixels to the total image *size*, $Frac3$, and the ratio of *length* to *size* called *Length over Size* (LoS) [18].

3.3.3 Longitudinal Time Profiles

While all parameters introduced in Section 3.3.2 are based on the 2D camera images, CT5 provides additional information about the image's time structure. An approach already tested by the HEGRA collaboration in 1999 for gamma-hadron separation using the time development of the shower image is described in [19]. The basic idea is again that γ-

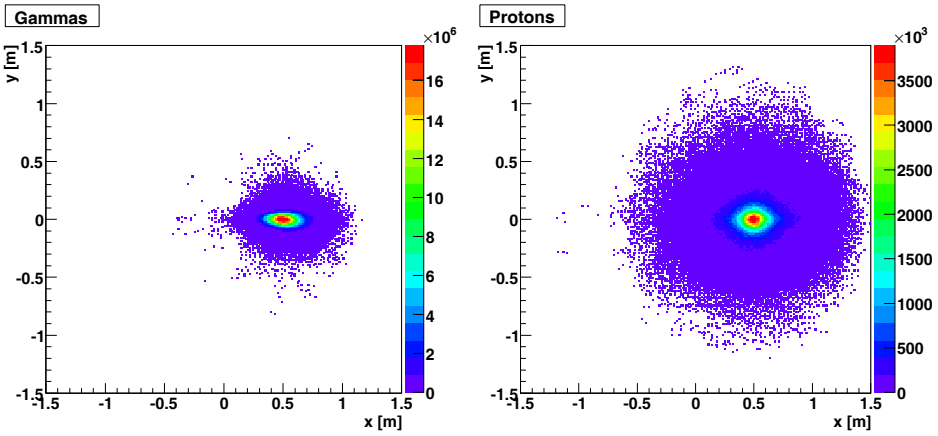

Fig. 3.12: *Overlay of camera images after allignment of their major axis along the camera system's x-axis and positioning of their CoG at (0.5,0). Again, one can see the larger width of proton images compared to γ-ray images.*

rays originate at the centre of the camera, which means that the beginning of the shower is imaged close to the camera centre, whereas its end is mapped at the camera's outer region. Hadronic showers, in contrast, can originate anywhere in the sky and should therefore develop differently.

Figure 3.11 shows the propagation of Cherenkov light into the telescope cameras for two different impact parameters. While the light mapped close to the camera centre is always emitted first, it may arrive in the camera after light emitted during the shower's further development. The reason for this is that the Cherenkov light travels with a velocity of $v = c/n$, where the refractive index n varies with the atmospheric height h, so that: $v = c/n(h)$.
In the case of an electromagnetic shower, however, the shower front travels at $v = c$ for a long distance. If the shower axis is close to the telescope (Figure 3.11, left side), the light emitted at the shower end will arrive before the light emitted in the upper atmosphere. For large impact parameters (Figure 3.11, right side) the situation is reversed and the light emitted at the shower start arrives first (due to the shorter path length). One would therefore expect to see different evolutions of γ-ray images along their major axis. For small impact parameters the image evolves from the camera edge towards the centre, for large impact parameters the image evolves just the other way round and for medium impact parameters the image evolves from the CoG towards the edge and the centre.

In principle, the longitudinal time-development of a camera image (called longitudinal profile) should therefore be suited to distinguish gammas from protons. In order to study these longitudinal profiles, all camera images are rotated in the camera coordinate system and then shifted along the x-axis of the camera system, until the CoG is located at (0.5,0). Subsequently, the image ist rotated around its CoG by the angle α, so that its major axis is alligned along the camera's x-axis. The intensity distribution of these transformed images in the camera system is shown in Figure 3.12. These images are then used to obtain a profile of the mean arrival time $\langle T0(x_0)\rangle$ as a function of the position on the major axis x_0 as well as the spread of $\langle T0(x_0)\rangle$:

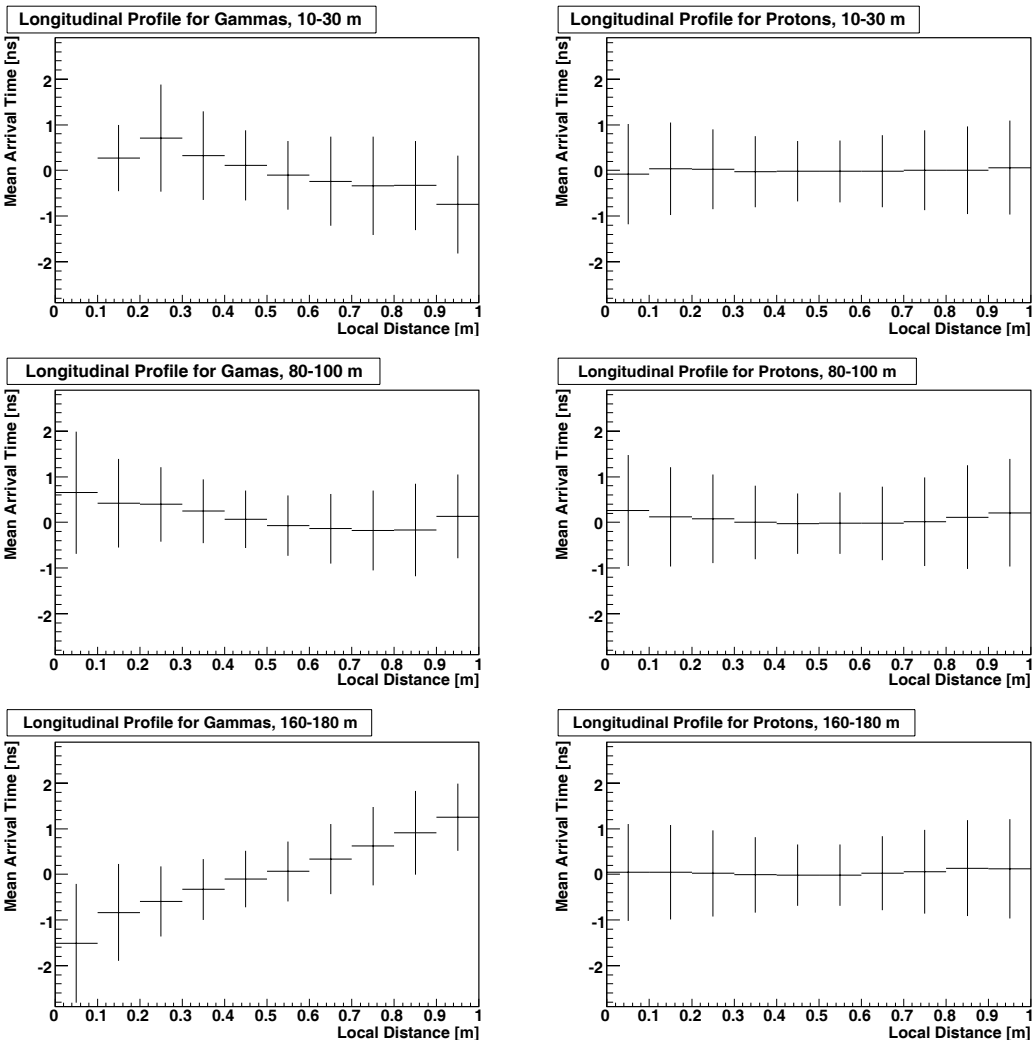

Fig. 3.13: *Longitudinal time profiles for gammas and protons for different impact parameter ranges. While the slope of the profile for gammas strongly depends on the impact parameter, the proton profiles show no pronounced dependency.*

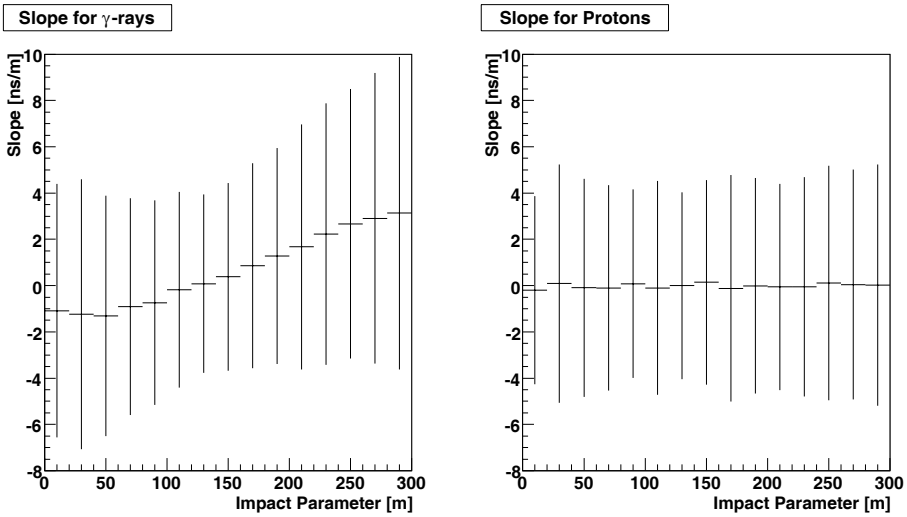

Fig. 3.14: *Mean slope of longitudinal gamma and proton profiles as a function of the impact parameter. In contrast to the proton profiles, the gamma profiles show a strong dependency of their slope on the impact parameter. The fluctuations of the slope are, however, larger than the change of slope itself.*

$$\langle T0(x_0)\rangle = \sum_{(pixels|x=x_0\pm\Delta x)} T0_{pix} - \langle T0\rangle, \tag{3.8}$$

where $\langle T0\rangle$ is the mean arrival time of the entire image. Figure 3.13 shows these profiles for different impact parameter ranges.

As expected, the profiles for gammas show a negative slope for small impact parameters, a positive slope for large impact parameters, and are curved for intermediate values of the impact parameter. This reflects the fact that for small distances the Cherenkov light emitted at the shower start arrives first, whereas for intermediate distances the light of both the shower beginning and end tends to arrive late. For large distances, the Cherenkov light arrives in the order of it's emission. The proton profiles on the other hand show no such clear structure. While this in principle could be used for gamma-hadron separation, the error bars of the profiles indicate that the spread due to shower fluctuations is larger than the effect itself.

Figure 3.14 confirms this assumption. It shows the average slope of the longitudinal profiles as a function of the impact parameter. While the slope increases linearly with the impact parameter for gammas, its spread is larger than the change of the slope itself. For all impact parameter in the range of 0 to 300 m, the slope's spread covers the whole range of -4 to 4 ns/m, and only a small percentage exceeds this range even for large shower distances. The longitudinal profiles presented in this chapter have therefore no sensible use for gamma-hadron separation, due to the large fluctuations of electromagnetic showers.

3.3.4 TMVA

TMVA[2] is a software environment included in the ROOT[3] framework comprising various classification techniques like rectangular cut optimisation, boosted decision trees and neural networks . It therefore provides powerful separation algorithms which can be used for Gamma-Hadron separation. In this thesis, a Feed Forward MultiLayer Perceptron (MLP) neural network is used, which will be described in the following Sections.

The MLP Neural Network

Generally speaking an artificial neural network (ANN) consists of any collection of simulated interconnected neurons (which give a certain response to a given set of input signals). It can be put in a defined state by applying external signals to some input neurons while measuring the response of one (or some) output neurons. It can therefore be seen as a (possibly nonlinear) mapping from a space of input variables $x_1, ..., x_n$ onto a space of output variables $y_1, ...y_n$ [13]. The complexity of such a network can be greatly reduced by ordering the network in layers (MLP) and allowing only directional connection from one layer to the consecutive one (feed forward). The first layer is called input layer, the last one output layer and each one in between hidden layer.

For signal-background separation using N characteristic variables, the input layer consists of $N + 1$ neurons, one for each input variable, and one bias node. The output layer consists of only one neuron, whose output is called the neural net estimator y_{ANN}. It classifies events as either signal-like or background-like, where the desired output for signal events is one, and minus one for background events. Figure 3.15 depicts the layout of such an MLP neural netwok. Each connection between a neuron i in the layer $l-1$ and a neuron j in the layer l is given a weight w_{ij}^{l-1} with which the neuron output y_i^{l-1} is multiplied before it is used as input for the neuron (l, j). Figure 3.16 shows the data-processing mechanism of a single neuron (l, j) that has n input connections. Each neuronal output of the preceding layer is multiplied with the weight associated with the respective connection and used as input value for the neuron. The neuron response function ρ then maps the input values to the new neuron output value y_j^l. Often the neuron response function can be separated into a synapsis function $\kappa : \mathbb{R}^n \to \mathbb{R}$, and a neuron activation function $\alpha : \mathbb{R} \to \mathbb{R}$, so that $\rho = \alpha \circ \kappa$.

In TMVA, the synapsis function can have the following forms [13, page 64]:

$$\kappa : (y_1^l, ..., y_n^l | w_{0j}^l, ..., w_{nj}^l) \longmapsto \begin{cases} w_{0j}^l + \sum_{i=1}^n y_i^l w_{ij}^l & \text{Sum,} \\ w_{0j}^l + \sum_{i=1}^n \left(y_i^l w_{ij}^l \right)^2 & \text{Sum of squares,} \\ w_{0j}^l + \sum_{i=1}^n |y_i^l w_{ij}^l| & \text{Sum of absolutes,} \end{cases} \tag{3.9}$$

while the available neuron activation functions are:

[2] Toolkit for MultiVariate Analysis, for information see [13]
[3] for information see [20]

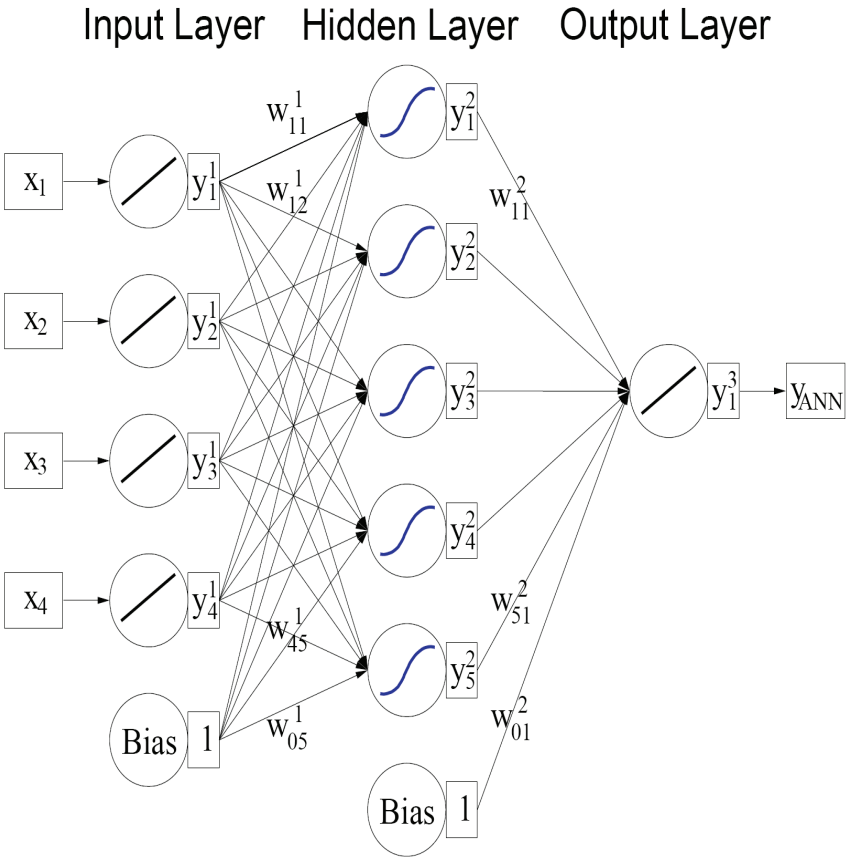

Fig. 3.15: *Exemplary layout of a feed forward MLP neural network with one hidden layer and a single output neuron. The neural network maps the input variables $x_1, \ldots, x_4$ to one output variable, the neural net estimator y_{ANN} (taken from [13]).*

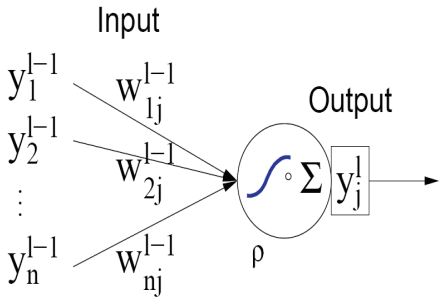

Fig. 3.16: *Data processing of a single neuron j in layer l with n input connections. Each output of one neuron of the preceding layer is mutliplied with a weight w_{ij}^{l} before being used as an input on the neuron response function $\rho : \mathbb{R}^n \rightarrow \mathbb{R}$ (taken from [13]).*

$$\alpha : x \longmapsto \begin{cases} x & \text{Linear,} \\ \frac{1}{1+\mathrm{e}^{-kx}} & \text{Sigmoid,} \\ \frac{\mathrm{e}^{x}-\mathrm{e}^{-x}}{\mathrm{e}^{x}+\mathrm{e}^{-x}} & \text{Tanh,} \\ \mathrm{e}^{-x^2/2} & \text{Radial.} \end{cases} \tag{3.10}$$

Training and Testing Neural Networks

Training of a neural network is done by adjusting the inter-connection weights until an optimal performance of the neural net classifier is reached. TMVA uses a supervised learning method (i.e. a training method, where each training event is known to be signal or background) called "back propagation". Starting with a random set of initial weights, the neural net estimator y_{ANN} is calculated for a set of N training events $\mathbf{x}_a = \{x_1, \ldots, x_n\}$ and then compared to the desired output $\hat{y}_a$. The error function E is given by:

$$E(\mathbf{x}_1, \ldots, \mathbf{x}_N|\mathbf{w}) = \sum_{a=1}^{N} E_a(\mathbf{x}_a|\mathbf{w}) = \sum_{a=1}^{N} \frac{1}{2}(y_{\mathrm{ANN},a} - \hat{y}_a)^2 \tag{3.11}$$

In order to find the set of weights that minimises the error function, the set of weights $\mathbf{w}$ is shifted in $\mathbf{w}$-space a small distance in the direction $-\nabla_{\mathbf{w}} E$:

$$\mathbf{w}^{(\rho+1)} = \mathbf{w}^{(\rho)} - \eta \nabla_{\mathbf{w}} E, \tag{3.12}$$

where the positive integer η denotes the learning rate. For well randomized samples, $\mathbf{w}$ can be updated after each training event. This method is called online learning (instead of bulk learning) and is the method used in TMVA.

After the classifier training, its performance is tested and evaluated. TMVA performs diverse checks of the classifier's performance and generates for example ROC curves (background rejection vs signal efficiency, where the background rejection is defined as one minus the background efficiency), as well as the classifier signal and background efficiencies as a function of the cut value on y_{ANN}[4]. This can be used to find a cut which maximises the quality factor. Furthermore, TMVA ranks the input variables according to their Importance I_i, which for the TMVA neural networks is defined by the sum of the weights-squared of the connections leaving the variable's input neuron times the square of the variables sample mean $\bar{x}_i$:

$$I_i = \bar{x}_i^2 \sum_{j=1}^{n_h} \left(w_{ij}^1\right)^2, \quad i = 1, \ldots, n_{\mathrm{var}}, \tag{3.13}$$

where n_h is the number of neurons in the first hidden layer.
One of the most important checks of the classifier's performance is a check for overtraining. Overtraining occurs when too many model parameters of a classifier are adjusted to too few data points [13, page 19]. It leads to a seeming increase in the classifier's performance on the training data, and to a decrease when tested on an independent test sample. A convenient way to check a classifier for overtraining is therefore to compare

[4] all events resulting in a value of y_{ANN} smaller than the cut value are considered to be background

its output distributions for the training and test sample and check both distributions for their equality.

4 Results for Gamma-Hadron Separation in the Mono Regime

In this section, the results of the use of the TMVA MLP neural network for gamma-hadron separation are presented. The attainable quality factor will be tested for the influence of the new image cleaning method, as well as for different preselection cuts (with or without a preselection cut on local distance). Furthermore, the new image cleaning method will be tested on its reliability, especially at low energies.

4.1 Improvements by the New Image Cleaning Method

This Section aims at comparing the results of the new image cleaning method and the standard one. The new algorithm's influence on direction reconstruction as well as the quality of its selection cuts will be tested and the results checked on their dependence on the camera sampling rate.

4.1.1 Direction Reconstruction

As mentioned in Section 3.3.2, the Hillas parameter α is a measure for the quality of the reconstructed shower direction. It describes the angular deviation of the reconstructed to the true image axis, which corresponds to the deviation of the reconstructed shower axis to the true one.

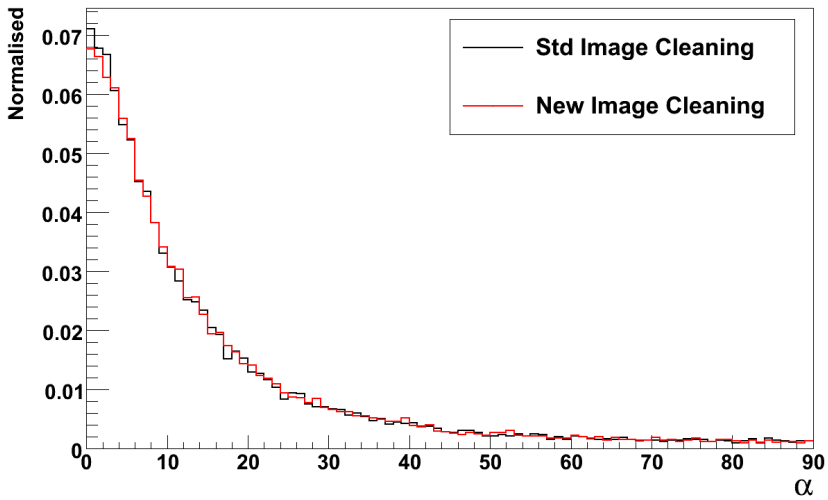

Fig. 4.1: *Distribution of the Hillas parameter α for standard and new image cleaning.*

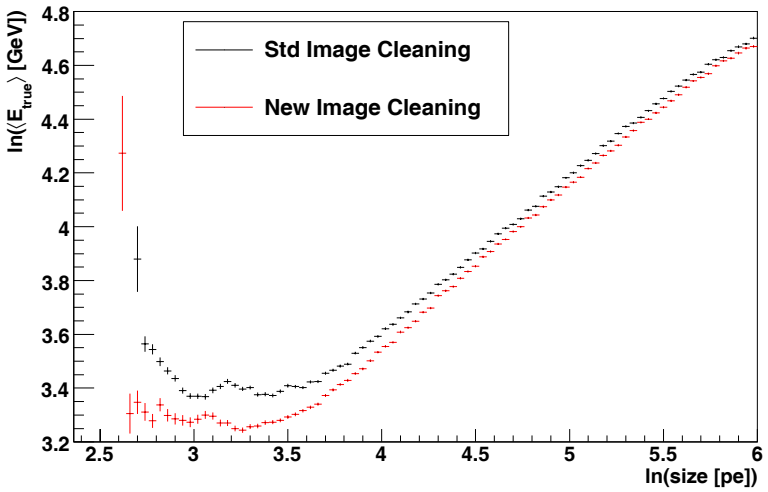

Fig. 4.2: *Logarithmic plot of mean true energy vs image size. For standard image cleaning* $\ln(\langle E_{true}\rangle)$ *is proportional to* $\ln(size)$ *down to* $\approx 35\,\mathrm{pe}$*. The new image cleaning leads to a better linearity for images smaller than* $35\,\mathrm{pe}$ *and to generally larger images at a given energy.*

Figure 4.1 shows the distribution of the α parameter of γ-ray events for standard and new image cleaning. As can be seen, both distributions agree very well with each other, which means that the new image cleaning method will have no influence on the quality of direction reconstruction.

4.1.2 Impact on the Energy Threshold

Without any background, the *size* of a camera image is proportional to the shower's energy. This relation is used to reconstruct the shower's energy, either directly via lookup tables (taking into account the dependency on the impact parameter) or any other algorithm. This relation, however, only holds for the true image *size*, i.e. the image *size* without image cleaning. For small images, too large a percentage of the shower's Cherenkov light is considered as background and wrongfully excluded from the reconstructed image. Figure 4.2 shows the mean true energy $\langle E_{true}\rangle$ as a function of the reconstructed image *size* for new and standard image cleaning. As can be seen, a linear relation exists between $\ln(\langle E_{true}\rangle)$ and $\ln(size)$ for a large part of the energy spectrum. For small images, however, too many signal pixels are possibly discarded from the image, resulting in a large variety of possible image *sizes* at a given shower energy. For standard image cleaning, any energy reconstruction below 35 pe would suffer from huge errors due to missing parts of the shower image. As can be seen in Figure 4.2, the linear regime for the new image cleaning method extends to lower image *sizes*. Furthermore, the average image *size* at a given shower energy is higher, resulting in a lower energy threshold of the telescope ($\langle E_{true}\rangle = 28\,\mathrm{GeV}$ instead of 31 GeV at an image *size* of 40 pe, which makes an effect of $\approx 10\%$ for small image *sizes*).

While the new image cleaning method accepts more pixels to the image, one needs to make sure that the selected pixel are part of the shower's true image, and not random fluctuations of the NSB. Figure 4.3 shows double logarithmic scatter plots of the shower's

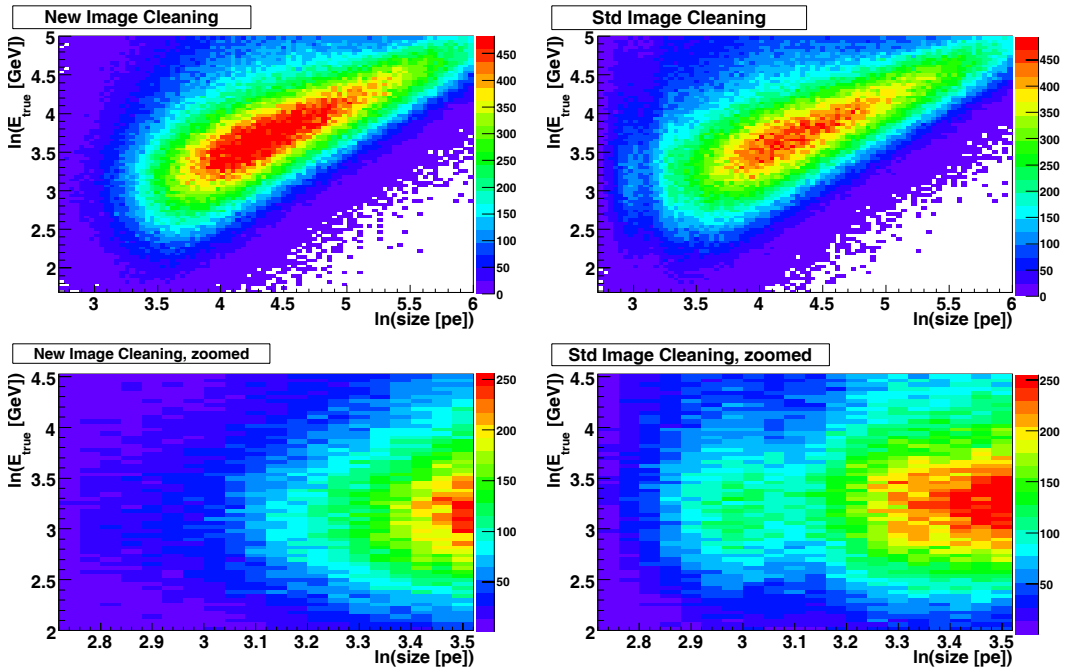

Fig. 4.3: *Scatterplots of* $\ln(E_{true})$ *vs* $\ln(size)$ *for standard and new image cleaning (upper row). The bottom row shows a zoomed view of the low energy and low size regime (*$E \in [7\,\mathrm{GeV}, 90\,\mathrm{GeV}]$, $size \in [14\,\mathrm{pe}, 35\,\mathrm{pe}]$*). While the standard image cleaning leads to images which are reconstructed with too low a size (right side), the new cleaning method results in a good reconstruction of the true image size even for very small images (left side).*

true energy vs the reconstructed image *size* for standard and new image cleaning. One can see that the standard image cleaning leads to a more irregular shape especially in the low energy and low *size* domain. The bottom row shows a zoomed image of the low *size* domain where one can clearly see an irregular bulge extending to low *sizes* for the standard image cleaning (right side), which results from the elimination of too many pixels from the image. The new image cleaning method shows no such distortion (left side), which means that the additional pixels included in the image are indeed part of the true shower image.

Figure 4.4 shows a smoothed scatter plot for the standard image cleaning overlaid with the contours of the new cleaning. Again one can see the more regular shape generated by the new cleaning algorithm.

4.1.3 Influence of a Different Time Resolution

The sampling rate of the H.E.S.S. II camera can be varied between 500 MHz and 3 GHz (see Section 2.2). In the Monte-Carlo simulations used in this thesis it is assumed to be 1 GHz, leading to a maximum time resolution of $1/\sqrt{12}$ ns. It is therefore necessary to check the improvements by the new image cleaning presented in the preceding Section on their dependency on the time resolution. Figure 4.5 depicts the mean true energy as a function of image *size* for standard, as well as new image cleaning, assuming different sampling rates of 0.5, 1 and 2 GHz. As the graphs show only small fluctuations for different

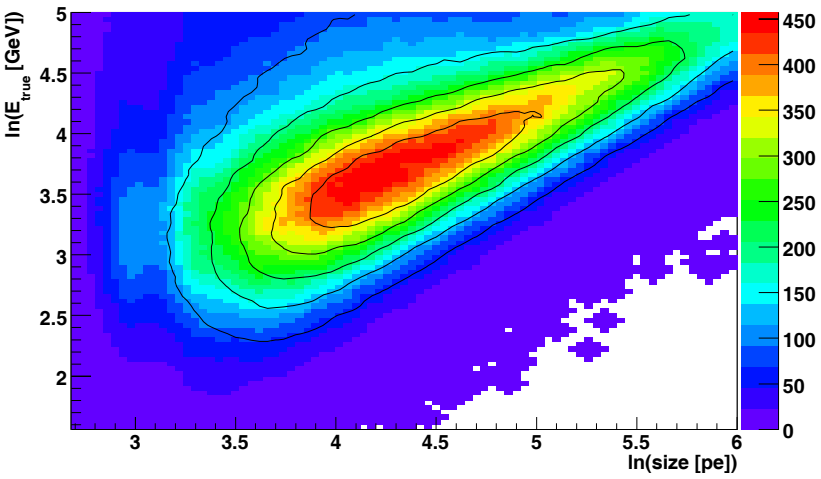

Fig. 4.4: *Smoothed scatterplot of* $\ln(E_{true})$ *vs* $\ln(size)$ *for standard image cleaning overlaid with the contours for new image cleaning.*

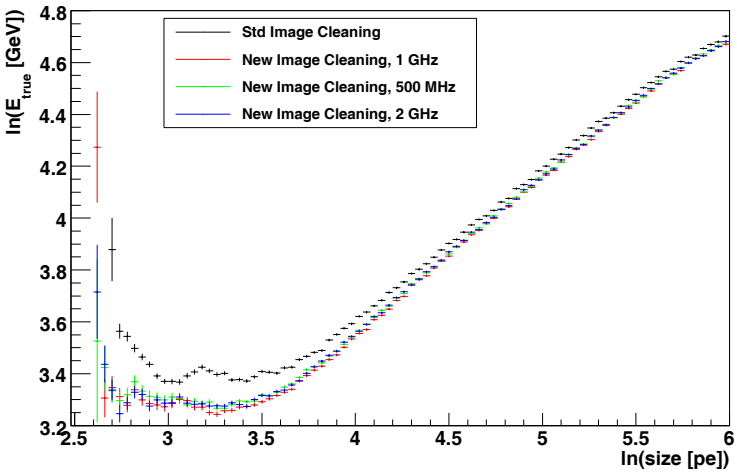

Fig. 4.5: *Dependency of the new image cleaning on the CT5 sampling rate.*

sampling rates, a changing time resolution has only little influence on all improvements resulting from the new cleaning algorithm.

4.2 Gamma-Hadron Separation using the MLP Neural Network

4.2.1 Input Parameters

Since longitudinal profiles are not suited to distinguish between γ-rays and protons, only the parameters described in Section 3.3.2 will be used as input variables for the neural network used for gamma-hadron separation in this thesis. Figure 4.6 shows the distributions of all input variables. Obviously, α is the best selection criterion for gamma-hadron separation of all input variables, while especially *LoS* (Length over Size) shows nearly identical distributions for signal and background.

Table 4.1 shows a ranking of all input variables according to their separation. α and the local distance show the largest separation, while *RSW* and *RSL* show smaller separation and $Frac3$, as well as *LoS*, a separation close to zero. The separation, however, does not take into account the correlation between the input variables. Figure 4.7 shows the linear correlation coefficients between the input variables for signal and background.

Input Variable	**Separation**
α	3.5e-01
Local Distance	3.1e-01
RSW	1.7e-01
RSL	1.6e-01
Frac3	9.9e-02
Length over Size	3.5e-02

Table 4.1: *Ranking of the TMVA input variables according to their separation.*

As can be seen, most variables are only weakly correlated. One discriminating criterion is the strong correlation for *RSW* and *RSL* for the background, whereas the correlation coefficient is ≈ 0 for signal events. While $Frac3$ is understandably anticorrelated with *RSW* & *RSL* (larger images lead to less intensity in the three brightest pixels compared to the whole image *size*), a further important point for signal-background separation is the strong correlation of *LoS* with *RSL* for signal events. Although *LoS* shows a separation close to zero and neural networks can even perform worse if given additional input parameters with small separation power, the correlation of *LoS* with the other input variables leads to an improved performance of the MLP network, when given as an additional input parameter. Therefore, all input variables presented in this Section, even $Frac3$ and *LoS*, will be used as input for the neural network used for gamma-hadron separation in the following Section.

4.2.2 Optimal Cut for Point Sources

The neural networks presented in the following Sections have been trained on a simulated point source with a spectral index of $\Gamma = 2.6$ and a simulated proton background with $\Gamma = 2.7$. After a preselection cut on the image *size* in order to select images which are still large enough to allow good reconstruction ($size > 40\,\mathrm{pe}$), 150 000 γ-ray events and

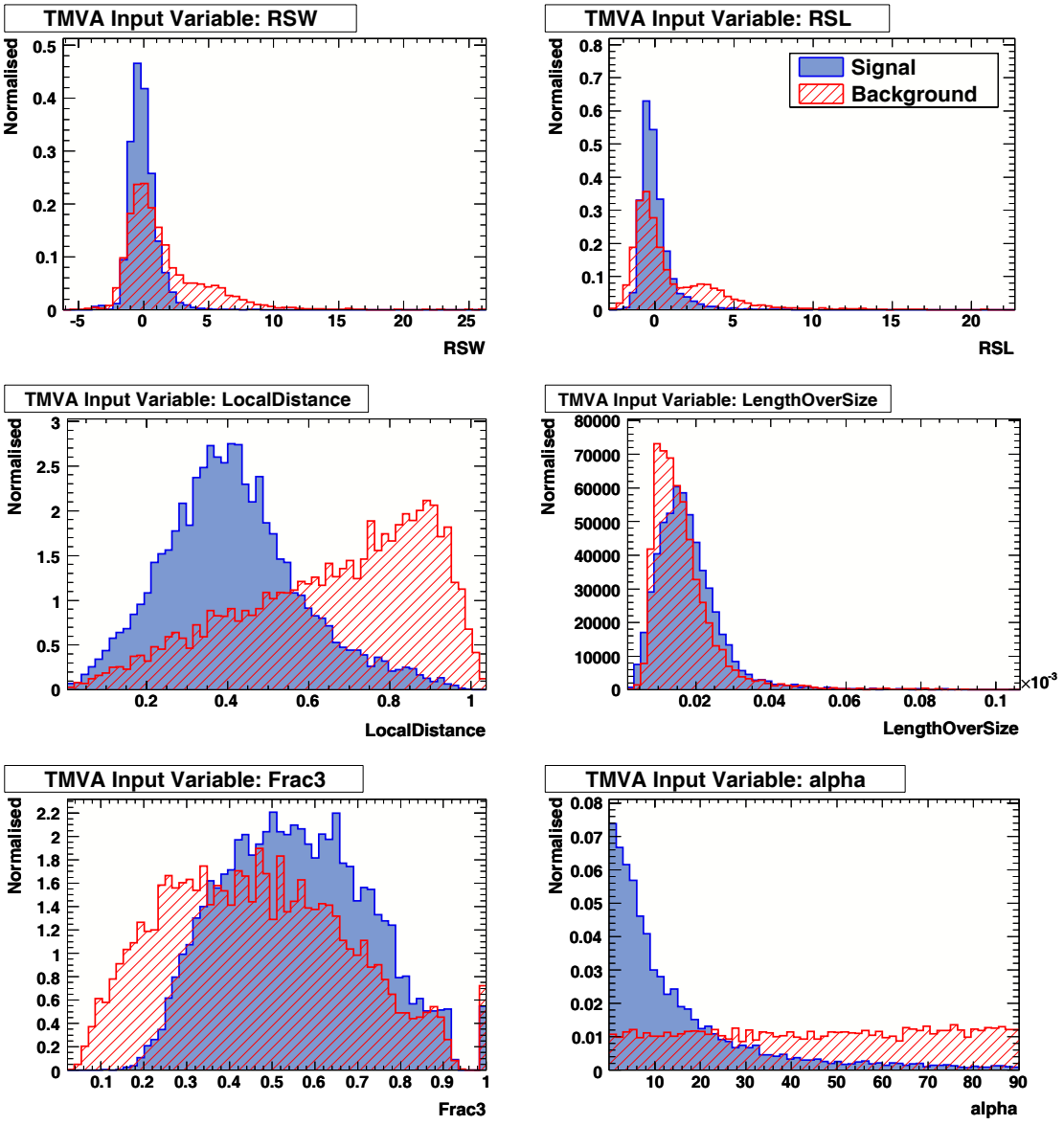

Fig. 4.6: *Distributions of the TMVA input variables.*

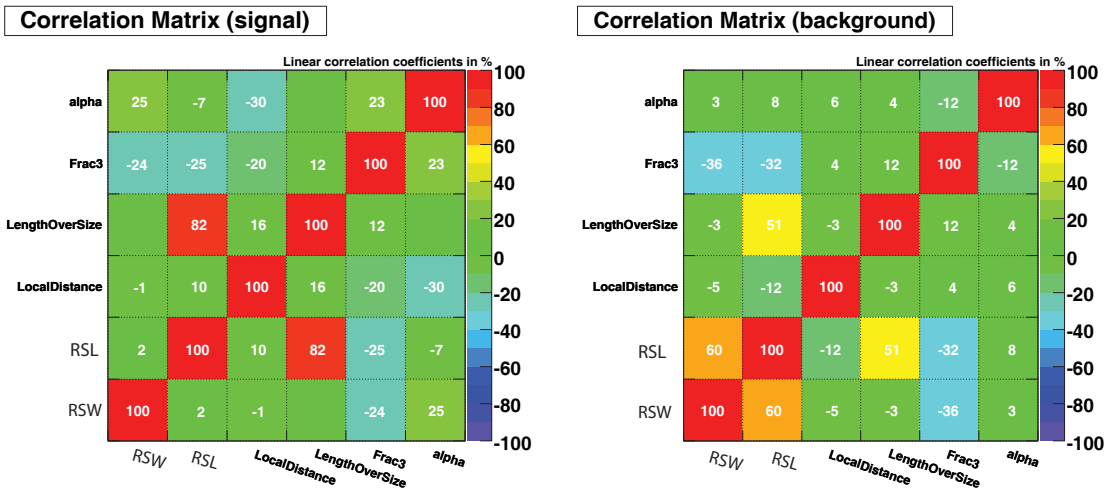

Fig. 4.7: *Linear correlation coefficients of the TMVA input variables.*

71 947 proton events are available for training and evaluation of the neural network. Out of these, 10 000 randomly selected events are used for network training, while the rest is used for evaluation. All variables are normalised to the range of $[-1, 1]$ before being used as input for the neural network.
The network itself consists of 2 hidden layers, each consisting of 37 and 22 neurons, with a Tanh neuron activation function and a Sum synapsis function (see Section 3.3.4). The network was trained in 550 training cycles with a learning rate of 0.02 (see Equation 3.12).

Optimal Quality Factor

For the new image cleaning described in Section 3.3.1, different classifiers were trained and tested on their performance. Figure 4.8 shows the ROC curve obtained from the trained MLP, Fisher and BDT (boosted desicion trees) classifier (for information on these classifiers see [13]). A classifier performs better if the area under the ROC curve is larger than for other classifiers. For the classifiers chosen in Figure 4.8, the MLP neural network and BDT (boosted decision trees) classifier perform equally well, while the Fisher classifier performs worse. Due to the generally faster and better performance of artificial neural nets compared to BDTs, however, the MLP neural net was chosen for gamma-hadron separation in this thesis.

A reasonable quantity on which a classifier should be optimised in γ-ray astronomy is the Quality Factor η, described in Section 3.1.2. Figure 4.9 shows the signal and background efficiency as a function of the cut on the MVA[1] classifier output, in this case the neural net estimator (compare Section 3.3.4). While the background efficiency drops sharply when cutting at -1, the signal efficiency stays close to 1 until ≈ 0. The pink curve shows the quality factor as a function of the MVA cut. A cut at 0.8868 maximises the quality factor, which is 4.44 at its maximum. The signal and background efficiencies at maximum are 0.56 and 0.016 respectively.

Figure 4.10 shows the MLP classifier's output distributions for signal and background events for the training and the test sample. As described in Section 3.3.4 this is a check

[1] multi variate analysis

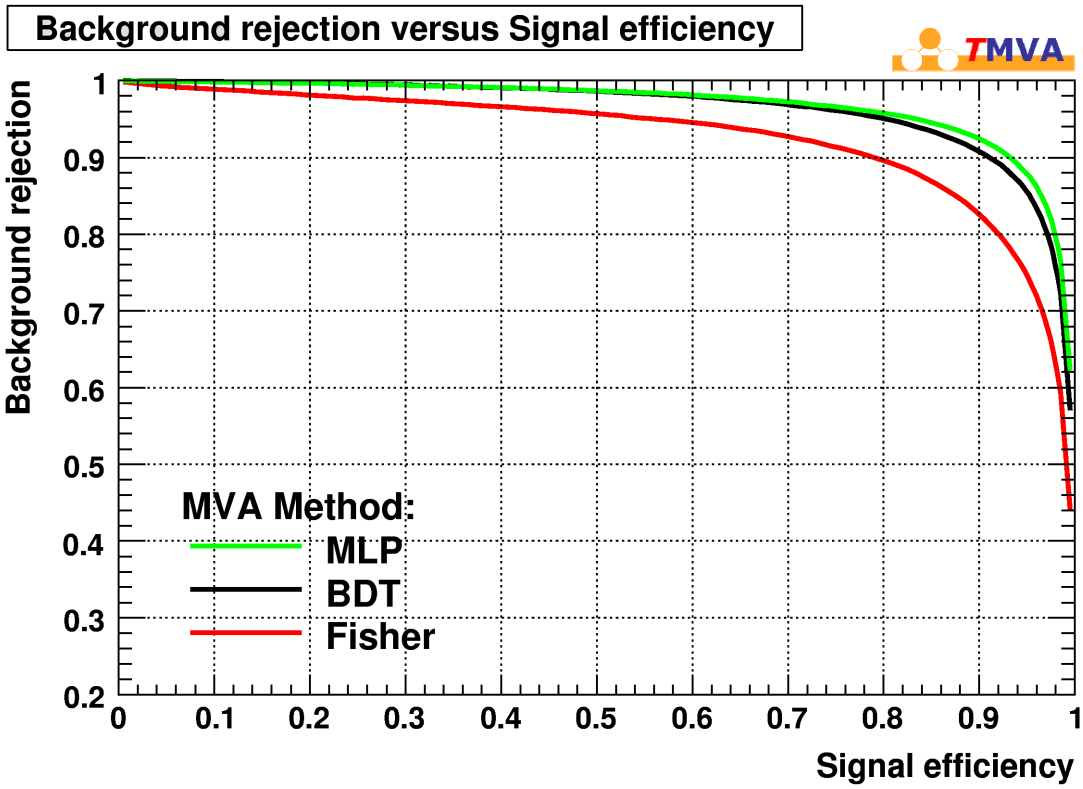

Fig. 4.8: *Background rejection vs signal efficiency for different MVA classifiers.*

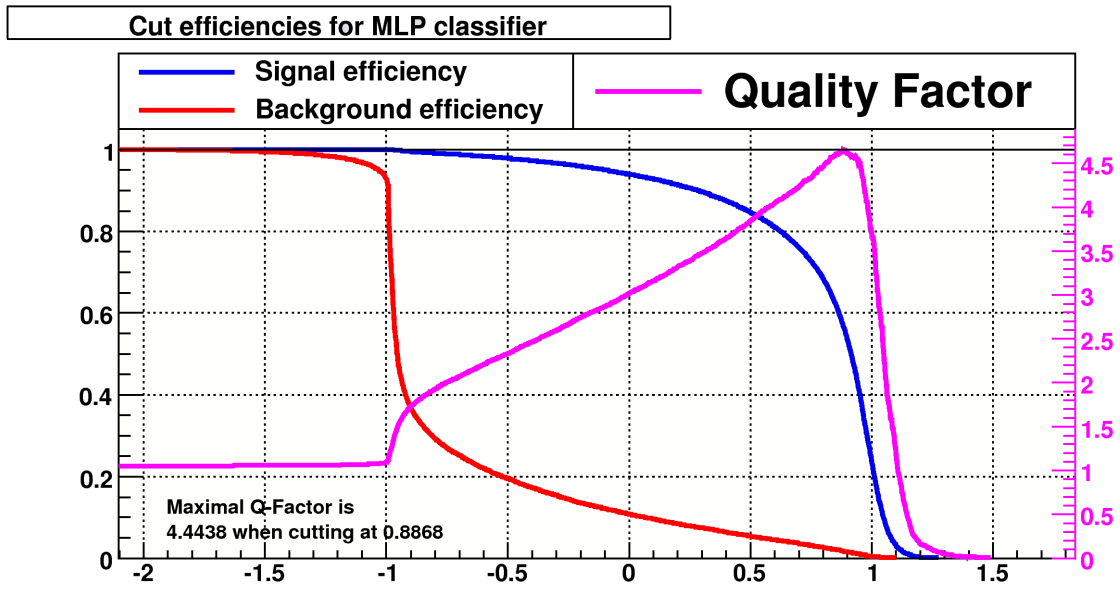

Fig. 4.9: *Signal and background efficiencies as well as the quality factor as a function of the MVA cut for new image cleaning.*

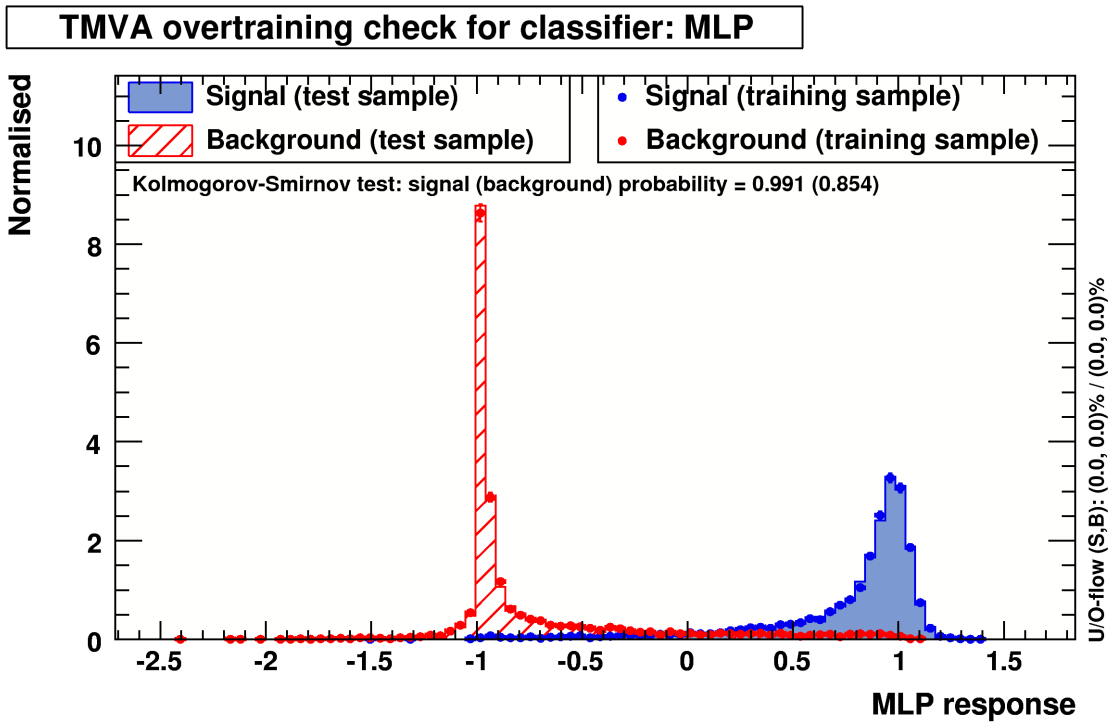

Fig. 4.10: *MLP ouput distributions for signal and background events of the training and test sample.*

on overtraining, as the distributions diverge when overtraining occurs. The Kolmogorov-Smirnov probability[2] that the training and test distributions are equal for signal (background) events is 0.991 (0.854), which means that no indication of overtraining is evident. Table 4.2 summarises the ranking of the different input variables according to their Importance as defined in Section 3.3.4, which differs somewhat from the ranking according to separation. The reason for this are the correlations between the input variables, as well as the fact that all variables with a nearly symmetric distribution around zero are ranked lower than variables with a strongly asymetric distribution, due to their smaller expectation value.

Rank	Variable	Importance
1	RSL	2.1e+02
2	Length over Size	1.5e+02
3	RSW	1.1e+02
4	alpha	2.5e+01
5	Local Distance	3.7e+00
6	Frac3	6.3e-01

Table 4.2: *Ranking of the MLP input variables according to their Importance.*

[2]for information on the Kolmogorov test, see for example [21]

Influence on the Energy Threshold

High-energy showers create predominantly large images, which usually allow a better discrimination of γ-rays and protons. Therefore, any gamma-hadron selection cut usually achieves its best results for high-energy events. In order to maximise their efficiency, most cuts reject mainly low-energy γ-ray events. This, in turn, causes a higher energy threshold of the system. The energy threshold can be defined as the maximum of the differential trigger rate (for information on the differential trigger rate and how to obtain the energy treshold, see for example [22]). Figure 4.11 shows the evolution of the energy threshold as a function of the MVA cut value. One can see that the MVA cut has almost no impact on the energy threshold, which remains $\approx 27\,\mathrm{GeV}$ for all cuts, even though a minimal increase of the energy threshold from 26 GeV up to 28 GeV can be observed.

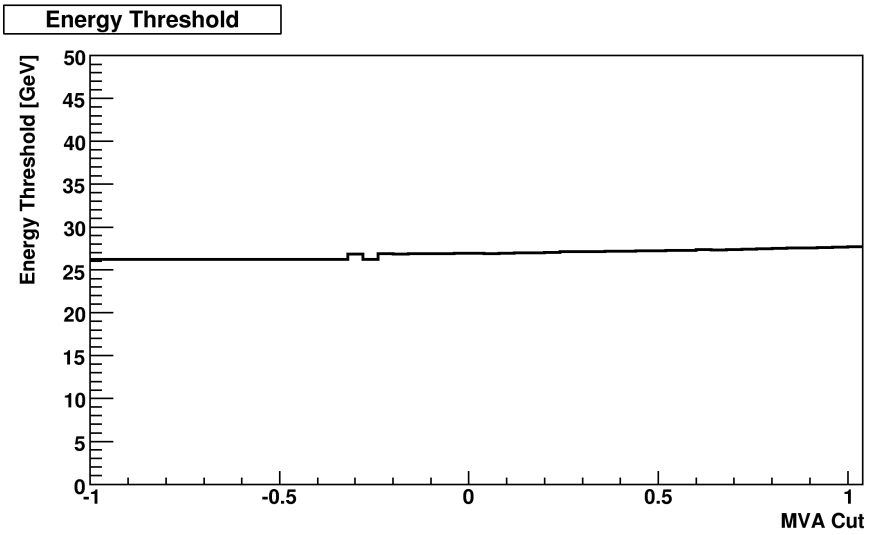

Fig. 4.11: *Energy threshold as a function of the cut on the MVA classifier.*

4.2.3 Influence of the New Image Cleaning

In order to examine the impact of the new cleaning method on gamma-hadron separation, a second neural net was trained and tested with the same events used in Section 4.2.2, which were processed with the standard tailcut image cleaning algorithm. Figure 4.12 shows the signal and background efficiencies of the neural net, as well as the corresponding quality factor as a function of the MVA cut. The resulting maximum quality factor is 3.79, when cutting at 0.8492. The corresponding signal and background efficiencies are 0.50 and 0.018 respectively. The new image cleaning therefore leads to an increase in the qualtity factor from 3.79 to 4.44, which is a gain of 17%.

4.2.4 Influence of a Cut on Local Distance

In the preceding Sections, the neccesity of an accurate direction reconstruction has not been considered. Images which are situated close to the camera edge suffer from the fact that part of the image might be outside the camera's field of view, while images situated too close to the centre suffer from having too round a shape (due to the mapping of the

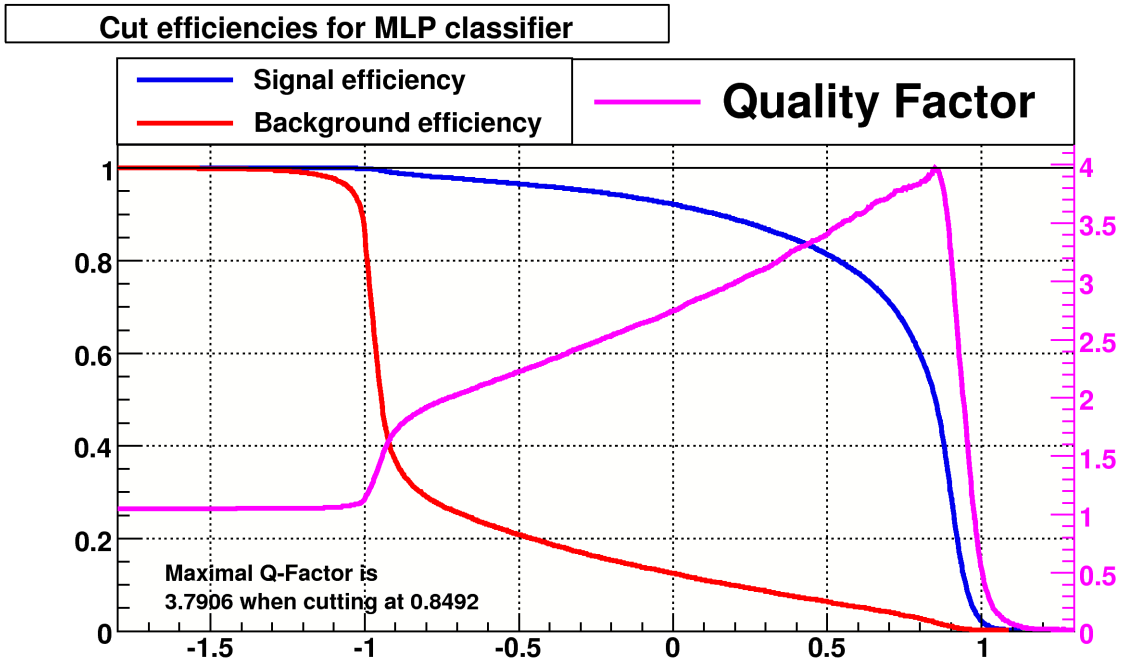

Fig. 4.12: *Quality Factor as a function of the MVA cut for standard image cleaning*

shower into the telescope camera). For both cases the reconstruction of the major axis and therefore of the shower's source becomes inaccurate. Therefore it is reasonable to perform a preselection cut on the local distance. The cut used in this thesis is:

$$0.29\,\mathrm{m} < \text{local distance} < 0.65\,\mathrm{m}$$

This corresponds to a cut on the angular distance in the field of view of $0.45° <$ angular distance $< 1°$, which was chosen in order to compare the results with the results obtained in an internal note on mono reconstruction stragey. Figure 4.13 shows the distribution of α before cuts, after the MVA cut presented in Section 4.2.2 and after both MVA and preselection cut on local distance.

Without cuts the distribution of α shows a RMS spread of 17°. After MVA cuts, where a large value of α is a strong indication for a proton shower, the RMS is already reduced to 13°. The preselection cut on the local distance, however, leads to a far smaller RMS of only 4°, which translates to a far better direction reconstruction. The preselection cut is therefore neccesary in order to achieve a sensible accuracy of the direction reconstruction.

The preselection cut on local distance understandably leads to a smaller quality factor of the MLP classifier, as a large local distance is of course a characteristic of proton showers. Figure 4.14 shows the results obtained by training the MLP network with events passing the local distance preselection cut. The maximal quality factor obtained, η_1, is only 3.37 instead of 4.44. Of course one needs to consider that the preselection cut on the local distance also leads to a better signal to noise ratio. The quality factor of the preselection cut η_2 is ≈ 1.14. As can be seen from the definition of the quality factor: $\eta = \hat{S}/S$, the overall quality factor η_{new} of both local distance preselection and MVA cut is the product of both quality factors:

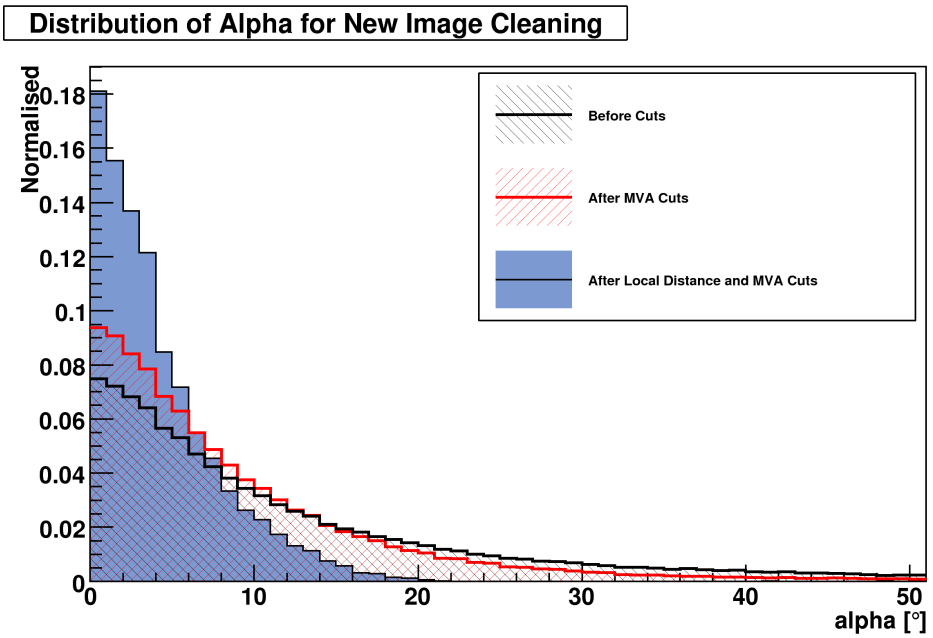

Fig. 4.13: *Distributions of the α parameter for new image cleaning without cuts, after MVA cut as well as after local distance and MVA cut.*

$$\eta_{\text{new}} = \eta_1 \cdot \eta_2 = 3.9.$$

This is still $\approx 12\%$ less than the quality factor without local distance preselection cuts. Considering, however, the importance of an accurate direction reconstruction and the possibility of a successive θ^2 cut, a preselection cut on local distance is neccesary and could even lead to an overall gain in the quality factor due to the increased performance of a θ^2 cut, as less γ-rays are reconstructed at a large angular distance from the camera centre and excluded from the analysis.

For standard image cleaning the decrease in the quality factor is less than for the new cleaning. Figure 4.15 shows the quality factor obtainable with an MLP classifier. The optimal quality factor is 3.11, which together with a quality factor for the local distance preselection cut of 1.17 yields an overall quality factor of:

$$\eta_{\text{std}} = 3.64,$$

which is only 4% less than the one obtained without the local distance preselection cut, compared to 12% for the new image cleaning method. The new cleaning method, while being more sensitive to a local distance cut, however, still yields a larger quality factor and exceeds the quality factor for standard cleaning by 8%.

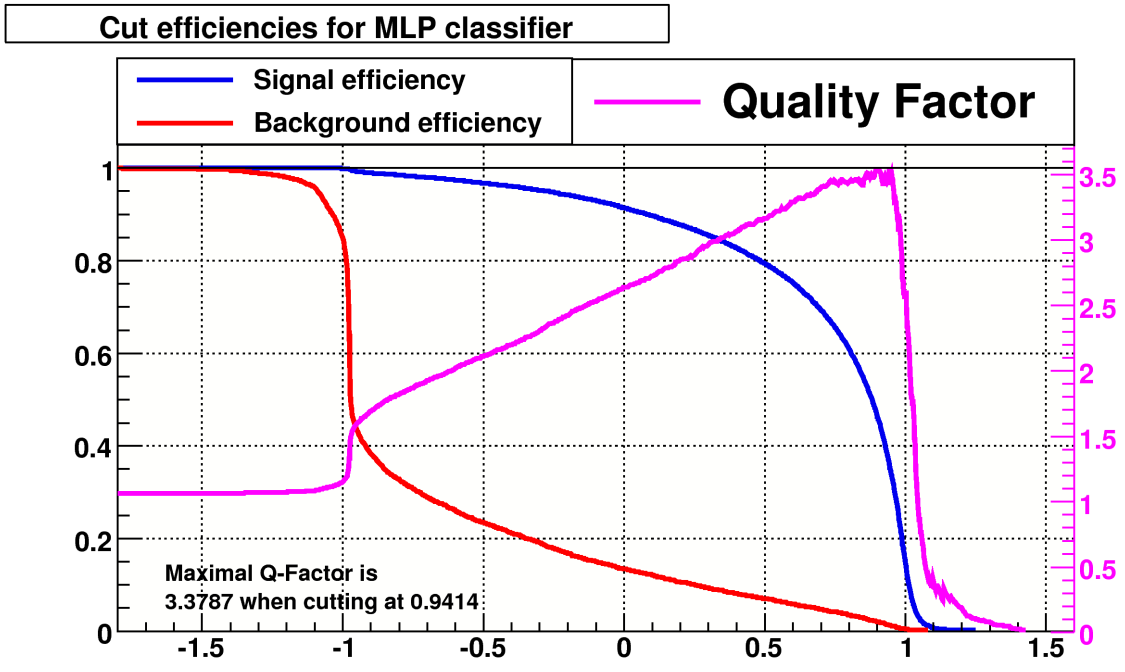

Fig. 4.14: *Quality Factor for new image cleaning as a function of the MVA cut after local distance preselection cuts.*

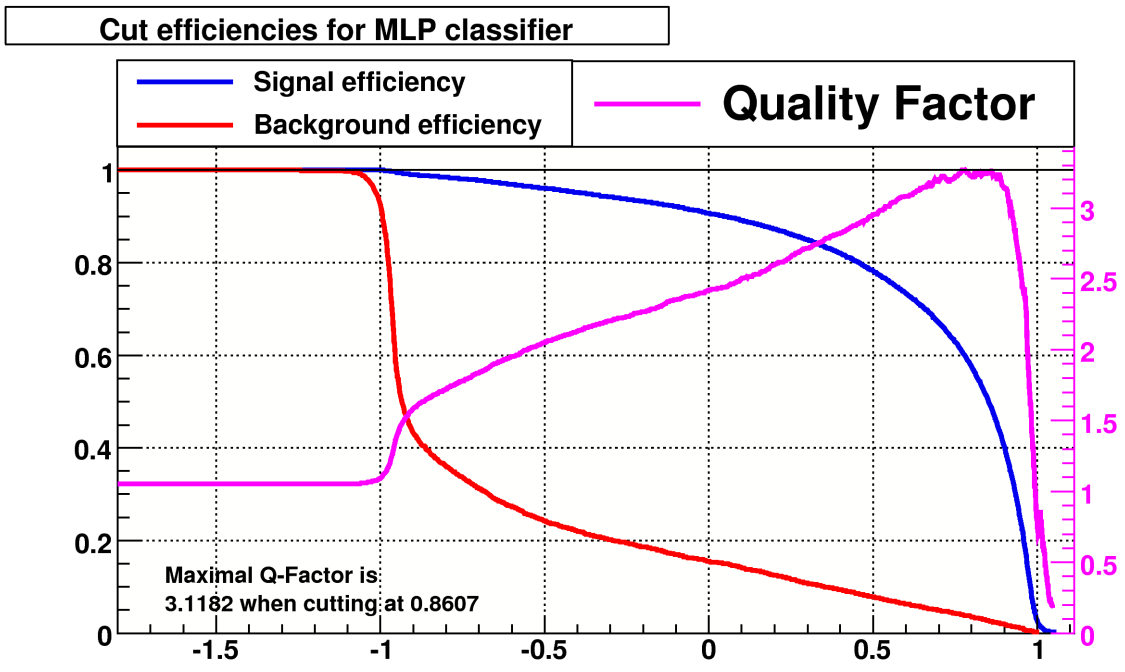

Fig. 4.15: *Quality Factor for standard image cleaning as a function of the MVA cut after local distance preselection cuts.*

5 Conclusion and Outlook

In this work, different methods for gamma-hadron separation were tested on their suitability for H.E.S.S. II mono events. Special attention was given to the use of pixel timing information for gamma-hadron separation. The methods which showed good performance were optimised on a simulated point like source with a spectral index of 2.6, and the influence of the different methods investigated.

In a first step, a new image cleaning was adopted, which considers not only the topological information of a camera image, but also the image's time structure. The new image cleaning method leads to a more complete reconstruction of the true shower image for small images, which is of special importance for the low-energy mono regime. At the same time, the new method was shown to have no impact on the accuracy of direction reconstruction, while leading to a lower energy threshold of the system due to the additional pixels kept in the reconstructed image.

In the next step, supplementary to the variables used for gamma-hadron separation for stereoscopic H.E.S.S. I events, additional variables were introduced: the ratio of image *length* to image *size* called *Length over Size* and the fraction of the total image *size* contained in the three brightest pixels called $Frac3$ are used to obtain a better gamma-hadron separation. Moreover, the applicability of longitudinal time profiles was tested, but due to the strong fluctuations of air showers they were not used for gamma-hadron separation.

In a final step, the discriminating variables were used as input for a feed forward multilayer perceptron neural network in order to achieve an optimal performance, i.e. an optimal quality factor. The best quality factor achieved was 4.44, where only a preselection cut of $size > 40\,\mathrm{pe}$ was applied. The gain in the quality factor, contributed by the new image cleaning method was shown to be 17%. The gamma-hadron separation cut on the neural network output was shown to have no influence on the energy threshold of the telescope. In order to achieve a better accuracy of the reconstructed direction, a further preselection cut on the local distance is needed. Although this cut is neccessary, the preselection cut leads to a reduced quality factor of 3.38. While being more sensitive to such a preselection cut, the new image cleaning still leads to a gain of 8% in the achievable quality factor compared to the standard H.E.S.S. I image cleaning.

The work done in this thesis has shown that the timing information of the CT5 camera is suited to improve gamma-hadron separation. As, however, the single most important point for stereoscopic gamma-hadron separation is the cut on θ^2, it is desirable to investigate the separation power of such a cut for mono events, as soon as a final direction reconstruction algorithm has been decided on. Furthermore, the image cleaning method is not yet fully optimised - due to ten independent parameters, and due to the dependance of the optimal threshold values on the intensity of the night sky background. In order to do that, new Monte-Carlo simulations have to be generated for different NSB photon rates. Moreover, the necessity of a preselection cut on the image *size* should be investigated as soon as all analysis procedures have been decided on.

List of Figures

List of Tables

Bibliography

[1] H.E.S.S. Experiment Homepage. `http://www.mpi-hd.mpg.de/hfm/HESS/`, November 2008.

[2] M. S. Longair. *High energy astrophysics*, volume 1, "Particles, photons and their detection". Cambridge University Press, 2nd edition, 2004.

[3] F Aharonian, J Buckley, T Kifune, and G Sinnis. High energy astrophysics with ground-based gamma ray detectors. *Reports on Progress in Physics*, 71(9):096901 (56pp), 2008.

[4] Homepage of the Fermi Gamma-ray Space Telescope. `http://fermi.gsfc.nasa.gov/science/`, November 2008.

[5] W.-M. Yao and et al. *Particle Physics Booklet.* paricle data group, July 2006.

[6] D. Berge. *Development of an Algorithm for the Shower Reconstruction with the H.E.S.S. Telescope System.* Diploma Thesis, Humboldt-Universität zu Berlin, November 2002.

[7] W. Heitler. *Quantum Theory of Radiation.* Dover Press, 3rd edition, 1954.

[8] D. Berge. *The gamma-ray supernova remnant RX J1713.7-3946 with H.E.S.S.* PhD thesis, Ruperto-Carola University of Heidelberg, February 2006.

[9] P. Vincent for the H.E.S.S. collaboration. H.E.S.S. Phase II. In *29th International Cosmic Ray Conference Pune*, volume 5, pages 163–166, 2005.

[10] R. Cornils and et al. The optical system of the h.e.s.s. ii telescope. In *29th International Cosmic Ray Conference Pune*, volume 00, pages 101–106, 2005.

[11] D. Heck and T. Pierog. *Extensive Air Shower Simulations with CORSIKA: A User's Guide.* Forschungszentrum Karlsruhe, November 2007.

[12] K. Bernloehr. CORSIKA and sim_ hessarray – Simulation of the Imaging Atmospheric Cerenkov Technique for the H.E.S.S. Experiment. *H.E.S.S. Internal Notes (unpubl.)*, April 2002.

[13] A. Hocker, P. Speckmayer, J. Stelzer, F. Tegenfeldt, H. Voss, K. Voss, A. Christov, S. Henrot-Versille, M. Jachowski, A. Krasznahorkay Jr., Y. Mahalalel, R. Ospanov, X. Prudent, M. Wolter, and A. Zemla. Tmva - toolkit for multivariate data analysis. 2007.

[14] T.-P. Li and Y.-Q. Ma. Analysis methods for results in gamma-ray astronomy. *The Astrophysical Journal*, 272:317–324, September 1983.

[15] A. M. Hillas. Cerenkov light images of EAS produced by primary gamma rays and by nuclei. In F. C. Jones, editor, *International Cosmic Ray Conference*, volume 3 of *International Cosmic Ray Conference*, pages 445–448, August 1985.

[16] W. Benbow. The H.E.S.S. standard analysis technique. Prepared for 7th Workshop on Towards a Network of Atmospheric Cherenkov Detectors 2005, Palaiseau, France, 27-29 Apr 2005.

[17] M. Shayduk and et al. A New Image Cleaning Method for the MAGIC Telescope. In *International Cosmic Ray Conference*, volume 5 of *International Cosmic Ray Conference*, pages 223–226, 2005.

[18] S. J. Gammell, B. Power-Mooney, D. J. Fegan, T. C. Weekes, and J. Quinn. Selection Strategies for Low Energy Events in Imaging Atmospheric Cherenkov Telescopes. In *International Cosmic Ray Conference*, volume 5 of *International Cosmic Ray Conference*, pages 2967–2970, July 2003.

[19] M. Heß and et al. The time structure of Cherenkov images generated by TeV γ-rays and by cosmic rays . *Astroparticle Physics*, 11:363–377, July 1999.

[20] R. Brun, F. Rademakers, P. Canal, I. Antcheva, and D. Buskulic. *The ROOT Users Guide 5.21*, December 2008.

[21] National Institute of Standards and Technology. `http://www.itl.nist.gov/div898/handbook/eda/section3/eda35g.htm`, November 2008.

[22] S. Schlenker. *Simulation Study of the H.E.S.S. Single Telescope Trigger Rate*. Diploma Thesis, Humboldt-Universität zu Berlin, September 2001.

Danksagung

An dieser Stelle möchte ich all jenen Danken, die mich bei den in dieser Arbeit vorgestellten Studien, sowie beim Verfassen der Arbeit unterstützt habe.

Zu allererst gilt mein Dank Herrn Professor Ch. Stegmann dafür, dass er es mir ermöglicht hat meine Diplomarbeit an seinem Lehrstuhl zu verfassen, und für seine große Fähigkeit seine Mitarbeiter zu motivieren.

Mein ganz besonderer Dank gilt vor allem Frau Dr. Ira Jung für die stetige Unterstützung und ihre Hilfsbereitschaft während des vergangenen Jahres.

Desweiteren Danke ich Herrn Dr. Oleg Kalekin für seine Hilfsbereitschaft sowie Herrn Daniel Göring und Herrn Tristan Nowak für ihre freundliche Unterstützung bei allen Programmierproblemen zu Anfang meiner Diplomarbeit. Herrn Fabian Schöck danke ich für seine wertvollen Ratschläge beim Korrekturlesen meiner Arbeit.

Schließlich möchte ich mich noch bei der gesamten Erlanger H.E.S.S. Gruppe für das aussergewöhnlich gute Arbeitsklima und das immer hilfsbereite Umfeld bedanken.

Erklärung

Hiermit bestätige ich, dass ich diese Arbeit selbstständig und nur unter Verwendung der angegebenen Hilfsmittel angefertigt habe.

Erlangen,

Martin Hupfer